Liquid Xenon Sloshing in Low Gravity Environments

Capstone Report

Hadrien Henriot, Jean Duthoit, Alexander Solakhyan

April 2026

Academic Integrity Pledge

We affirm that we are the sole authors of this report and we give due credit (i.e., use correct citations) to all used sources.

Hadrien Henriot **April 14, 2026**

Jean Duthoit

Jean Duthoit **April 14, 2026**

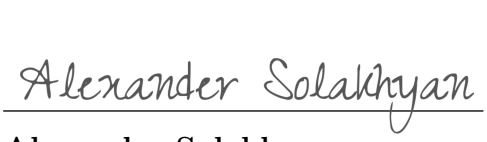

Alexander Solakhyan **April 14, 2026**

1 Executive Summary

The rising use of electric propulsion systems in satellites has increased reliance on xenon as a propellant. While Xenon's high atomic mass and favorable ionization properties make it ideal for propulsion, its storage presents a critical engineering challenge. Liquid xenon is susceptible to sloshing in microgravity conditions. During spacecraft reorientation maneuvers, oscillatory motion within partially filled tanks can generate destabilizing forces and moments, disrupt attitude control systems, increase corrective fuel consumption, and impose structural stress. To mitigate these risks, industry often considers supercritical xenon storage, which suppresses phase separation and simplifies fluid behavior. However, this approach requires significant energy input and complex thermal management. Determining whether liquid xenon storage is operationally viable is therefore both a technical and economic priority and is the main goal of the project. This project aims to quantify the effects of liquid xenon sloshing on spacecraft dynamics. The team developed analytical and numerical models to evaluate slosh-induced forces, moments, and center-of-mass displacement during representative satellite maneuvers. By coupling fluid motion with spacecraft attitude dynamics, the project identifies conditions under which sloshing meaningfully impacts stability and control performance. The results establish a predictive framework to assess risk levels and inform storage strategy decisions. Overall, the findings suggest that, under specific operational regimes, liquid storage may be feasible with appropriate control considerations and mitigation measures. Future work should include experimental validation of the models and integration with higher-fidelity attitude control simulations. Exploration of passive damping mechanisms, such as internal baffles or surface treatments could further reduce slosh effects without the energy burden of supercritical storage. This work contributes to more efficient satellite operations and supports informed design decisions in the growing electric propulsion market.

Contents

2 Introduction

Modern satellites, especially those using electric propulsion systems, often rely on liquid Xenon as a propellant. Its high atomic weight and inert behavior make it ideal for efficient long-duration propulsion. However, storing and managing cryogenic liquid in microgravity introduces a critical engineering challenge: sloshing. Sloshing refers to the oscillatory motion of liquid inside partially filled tanks. In the case of spacecrafts and satellites, it is often due to maneuvers performed to maintain the craft in a certain attitude or point its sensors towards a specific region of space.

In orbit, where there is little to no gravity to settle the liquid, sloshing can produce unpredictable forces and moments on the spacecraft. These forces interact with the satellite's control systems, potentially destabilizing orientation or leading to increased fuel consumption for corrective maneuvers. In addition, if unmitigated, sloshing can cause structural stress or cavitation in propellant lines, threatening mission success or shortening its lifetime.

In an effort to avoid those undesirable effects, industrials prefer to store Xenon in its supercritical form allowing to suppress the liquid and gas phases rendering the sloshing much easier to predict and mitigate. However, this alternative requires a lot of energy to heat up the gas and can prove difficult to implement as a result of the high heats and pressures required.

The purpose of this project, proposed by Airbus Defense and Space and led by UC Berkeley MEng students, is to quantify the effects of sloshing on the satellite in terms of forces, moments, and center-of-mass displacement and to understand how these dynamics influence the overall behavior of the spacecraft. By accurately characterizing these effects, we want to identify cases they may cause problems in and whether it is realistic to store Xenon in its liquid form or not.

Ultimately, this project seeks to provide insights into how liquid xenon sloshing impacts satellite stability and performance, enabling safer, more efficient satellite operations without relying exclusively on energy-intensive supercritical storage. To achieve this goal we have developed simple models to approximate the phenomenon, performed CFD simulations and designed an experiment to validate the model's outputs. Our resulting analysis demonstrates that slosh-induced attitude disturbances are minimal and fall well within the control authority of standard reaction wheels. Furthermore, the transient power required to counter these disturbances is vastly outweighed by the continuous thermal energy saved by avoiding supercritical heating. These results could guide both the design of future electric propulsion satellites and the development of control strategies that account for slosh dynamics, ensuring longer mission lifetimes, reduced propellant waste, and more reliable attitude control.

The global satellite propulsion market is projected to grow steadily over the next decade, driven by increased deployment of electric-propulsion spacecraft and extended mission lifetimes.[1] Xenon remains the primary propellant for Hall-effect and ion thrusters due to its high atomic mass and favorable ionization properties. As satellite operators seek to reduce mass, increase payload capacity, and extend operational life, Xenon's storage strategy directly impacts both

system efficiency and economic performance. Consequently, understanding whether liquid storage is viable under operational microgravity conditions is not only a technical challenge but also an industrial and strategic one.

3 Review of the literature

Sloshing in tanks is a topic that has been extensively studied by generations of engineers and researchers. Its critical impact on land, air, and space transportation has prompted large investments from industrial stakeholders and public institutions such as NASA and the European Space Agency. For this project we will only look at the work that has been done for space related applications which itself builds on previous studies for land applications.

Early foundational work in the 1960s, particularly during the Apollo and Saturn launch vehicle programs, established the theoretical basis for modeling liquid motion in accelerating containers. These studies demonstrated that propellant slosh can couple with vehicle structural modes and guidance systems, potentially leading to instability. Since then, slosh dynamics have been treated as a critical design consideration in launch vehicles, upper stages, aircraft fuel tanks, marine vessels, and spacecraft. [2]–[4]

In the space sector, research expanded further with the development of large cryogenic upper stages and long-duration spacecraft and satellite. Experimental campaigns conducted in drop towers, parabolic flights, and aboard the International Space Station have highlighted the unique challenges of low-gravity fluid behavior, including surface tension–dominated flow regimes and persistent oscillations. The development of numerical tools since the 1980s such as computational fluid dynamics (CFD), volume-of-fluid (VOF) methods, and coupled fluid–structure interaction models have drastically changed the approaches for predicting slosh-induced forces and moments with comprehensive simulations becoming the norm. [5]–[8]

Despite this extensive body of work, most classical slosh research focuses on common fluids (water, LOX, LH_2) and high-acceleration launch environments (behavior during launch not in microgravity). Comparatively fewer studies address cryogenic xenon behavior in microgravity during slow attitude maneuvers, which is precisely the operational regime of electric-propulsion satellites. As satellite missions grow longer and xenon tank volumes increase, the interaction between slosh dynamics and precision attitude control becomes increasingly relevant and motivates this study.

Thus, while the broader physics of sloshing is well established, there remains a gap in its application to liquid xenon storage for electric propulsion spacecraft. This project builds upon decades of theoretical, numerical, and experimental research, while targeting a specific operational context that is not yet fully characterized in the literature. [2], [3], [5]

From an industrial standpoint, alternative propellant management strategies compete with liquid storage. One approach consists in maintaining xenon in a supercritical or high-pressure gaseous state, eliminating phase separation and significantly reducing slosh-induced free-surface dynamics. While this configuration simplifies modeling and mitigates dynamic coupling, it introduces increased structural mass, higher tank pressures, and additional thermal management requirements. Other propulsion concepts, including iodine-based electric propulsion systems and hybrid chemical-electric architectures, further diversify the design landscape. These al-

ternatives illustrate that liquid xenon storage is not an isolated technical choice but part of a broader trade space involving mass efficiency, energy consumption, structural complexity, and operational stability. [9], [10]

4 Objectives and Methods

This section defines the objectives of the project, associated performance metrics, and the methodology used to address them.

4.1 Project objectives and metrics

While sloshing has been extensively studied for high-acceleration propulsion systems, its behavior for liquid xenon in microgravity during low-thrust maneuvers remains less documented. This study focuses on the coupling between sloshing dynamics and spacecraft attitude under such conditions.

The approach is structured around three key aspects:

- **Geometry- and regime-specific modeling**: two representative tank geometries are considered under low-acceleration translational and rotational maneuvers.
- **Fluid-specific analysis**: the study focuses exclusively on xenon, accounting for its thermophysical properties.
- **Attitude coupling**: sloshing is analyzed through its impact on spacecraft dynamics.

The objectives of this project are:

- Characterize liquid xenon sloshing dynamics in microgravity.
- Develop analytical models to estimate induced forces, moments, and center-of-mass displacement.
- Validate these models using CFD simulations.
- Quantify the impact of sloshing on spacecraft attitude.
- Design a reduced-gravity experiment for validation.
- Assess the feasibility of liquid xenon storage.

To evaluate feasibility, the following performance metrics are considered:

- Displacement of the liquid center of mass,
- Forces and moments exerted on the tank,
- Resulting perturbations in spacecraft angular velocity and pointing accuracy.

4.2 Technical approach

To address these objectives, an iterative approach combining analytical modeling, numerical simulations, and system-level analysis is adopted.

Analytical model Sloshing is modeled using an equivalent mass–spring system to approximate dominant modes and associated forces. This provides a computationally efficient reference for comparison with high-fidelity simulations [2],[4].

High-fidelity simulations Numerical simulations are performed using ANSYS Fluent and SimScale to capture free-surface dynamics under microgravity conditions. Both bubble-dominated and flat-interface configurations are considered, along with representative maneuver-induced accelerations.

Forces, moments, and center-of-mass motion are extracted and compared with analytical predictions, and used to estimate their impact on spacecraft attitude.

Data analysis: attitude effects The validated sloshing models are integrated into a spacecraft dynamics framework to quantify their effect on attitude. The resulting perturbations are evaluated against control system tolerances.

Experimental design An experimental setup is designed to support model validation in reduced-gravity conditions. The design is developed using CAD tools and driven by requirements linked to microgravity environment testing.

Economic analysis An economic assessment is conducted to evaluate the trade-offs between liquid and supercritical xenon storage, considering energy consumption, system mass, and operational constraints.

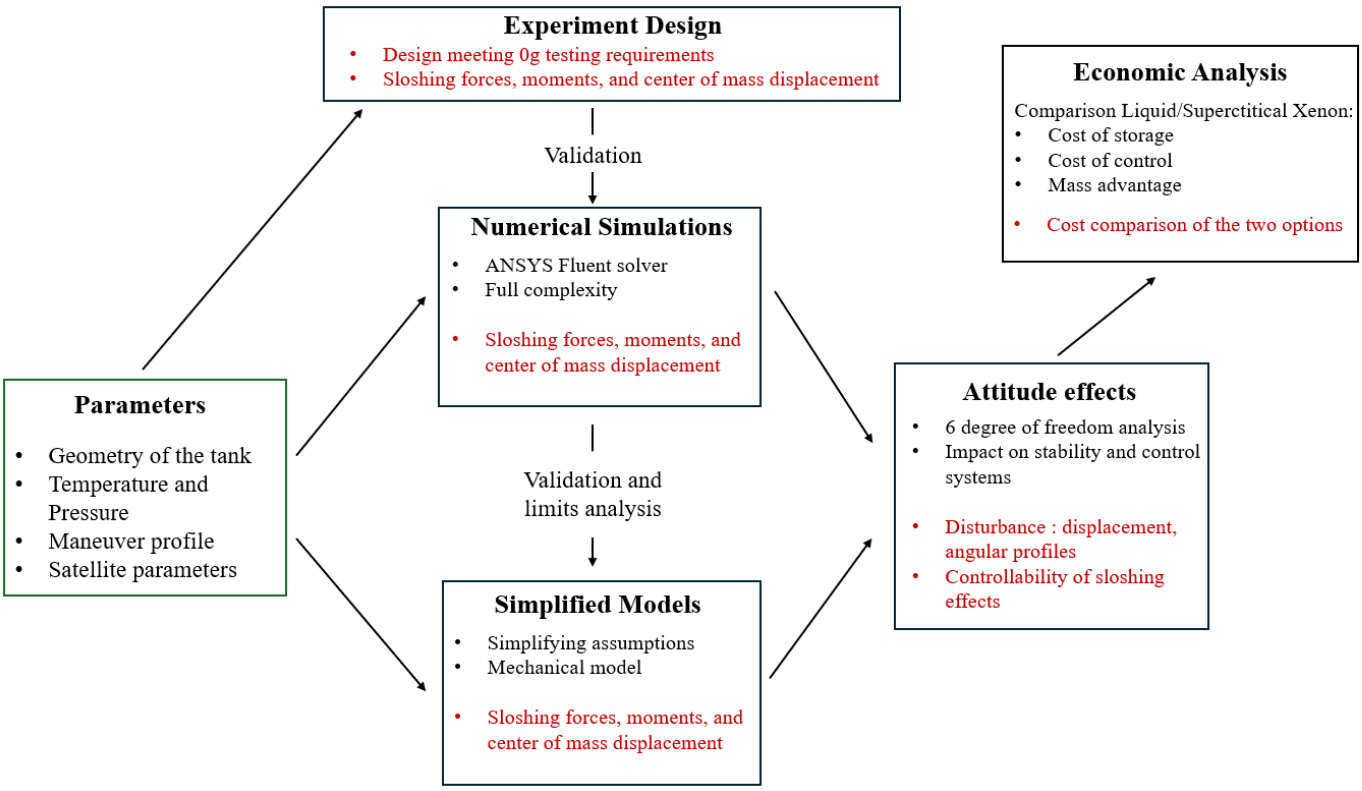

Figure 1: Diagram of the full process developed for the project. The outputs appear in red and inputs are boxed in green.

5 Problem Parameters and global hypothesis

This section defines the main assumptions, geometry, and operating conditions: microgravity environment, xenon thermodynamic state, satellite properties, tank geometries, and maneuvers.

5.1 Microgravity

The spacecraft operates in Low Earth Orbit (LEO), where it is in continuous free fall, producing microgravity conditions. Typical residual accelerations, often called *g-jitter*, arise from environmental disturbances such as:

- attitude control maneuvers,
- onboard mechanical vibrations,
- thruster firings,
- gravitational perturbations.

These accelerations are generally in the range of $10^{-6}g$ to $10^{-3}g$, where $g = 9.81\,\mathrm{m/s^2}$ is the standard gravitational acceleration.

5.2 Xenon working points

The section aims at determining a physically consistent operating point for a liquid–vapor equilibrium of xenon in the tank.

The tank has a fixed total volume:

$$V_{\text{tank}} = 20\,\text{L} \tag{1}$$

with a total xenon mass m_{Xe}, which may exist in liquid or vapor phases.

Thermodynamic properties of xenon are obtained from the NIST database using the miniREFPROP interface.

The specific volume of xenon in the tank is defined as:

$$v = \frac{V_{\text{tank}}}{m_{\text{Xe}}} \tag{2}$$

For a fixed tank volume and xenon mass, this value remains constant and allows the thermodynamic state to be located on a pressure–volume (PV) diagram (Figure 3).

Using the xenon PV diagram (Figure 3), the equilibrium state at a given temperature is determined by selecting the corresponding isothermal curve and locating the point associated with the system's specific volume v.

If the state lies within the saturation dome (two-phase region), the vapor quality x (mass fraction of vapor) is computed as:

$$x = \frac{v - v_l}{v_v - v_l} \tag{3}$$

where:

- v_l is the saturated liquid specific volume,
- v_v is the saturated vapor specific volume.

These values are obtained from saturation data at the specified temperature.

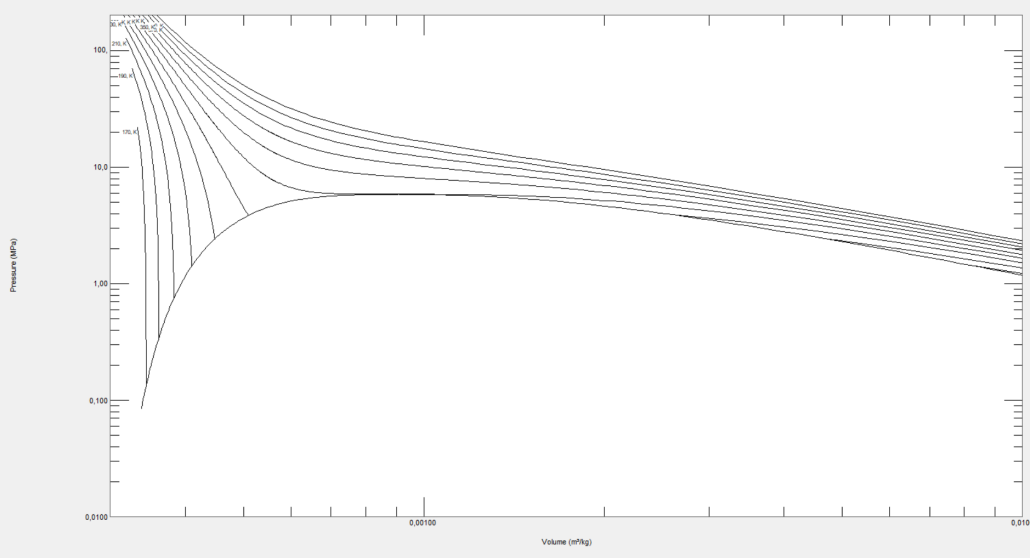

Figure 2: Pressure–volume (PV) diagram of xenon.

The entire process is automated using a Python algorithm coupled with NIST data. The algorithm:

- retrieves saturation properties,
- computes the specific volume,
- determines the thermodynamic region,
- calculates the vapor quality when the system is in the two-phase region.

Running the algorithm for different masses of xenon in the tank we can get an idea of how the situation will evolve through out the mission (as the mass of Xenon decreases).

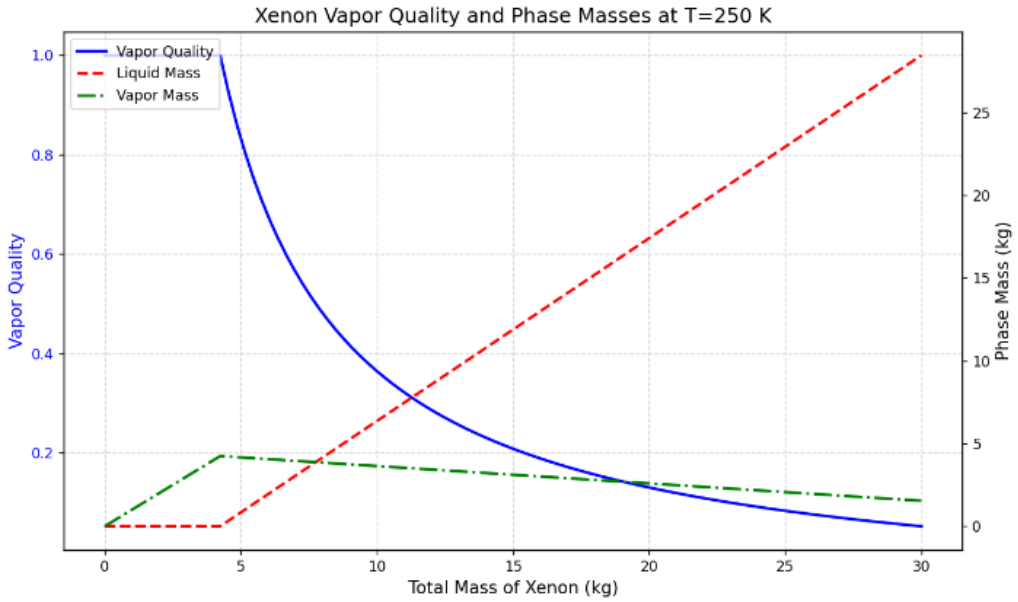

Figure 3: Vapor quality of xenon along with liquid and vapor mass as a function of total mass for a fixed temperature of T=250K

In this study we will concentrate on the situation where liquid is in equilibrium with its vapor. We choose for the rest of the study a working temperature of T=270K for which we have the following properties:

Property	**Symbol**	**Value**
Liquid density	ρ_l	1962.2 kg m^{-3}
Vapor density	ρ_v	376.6 kg m^{-3}
Surface tension	σ	1.8e-3 N m^{-1}
Liquid viscosity	μ_l	108e-6 Pa s
Vapor viscosity	μ_v	25e-6 Pa s

For general purposes we will suppose the tank is half filled with liquid the other half being vapor which gives us a total mass of $m_{Xe} = 23.38$kg of Xenon in the tank.

5.3 Satellite's configuration and parameters

The reference satellite for this study is the ARROW150 satellite from Airbus US Space and Defense. The satellite is classified as a "small sat"', and has a nominal orbit altitude ranges from 500km to 1500km in Low Earth Orbit range. For the purpose of the study, the satellite will be modeled assuming a full payload, with a total mass of 205.112 kg. A simple CAD model was created to create an inertia estimate of the satellite, shown below.

$$I = \begin{bmatrix} 36.25 & 0 & 0 \\ 0 & 29.7478 & 0 \\ 0 & 0 & 44.8639 \end{bmatrix} \text{kg} \cdot \text{m}^2 \tag{4}$$

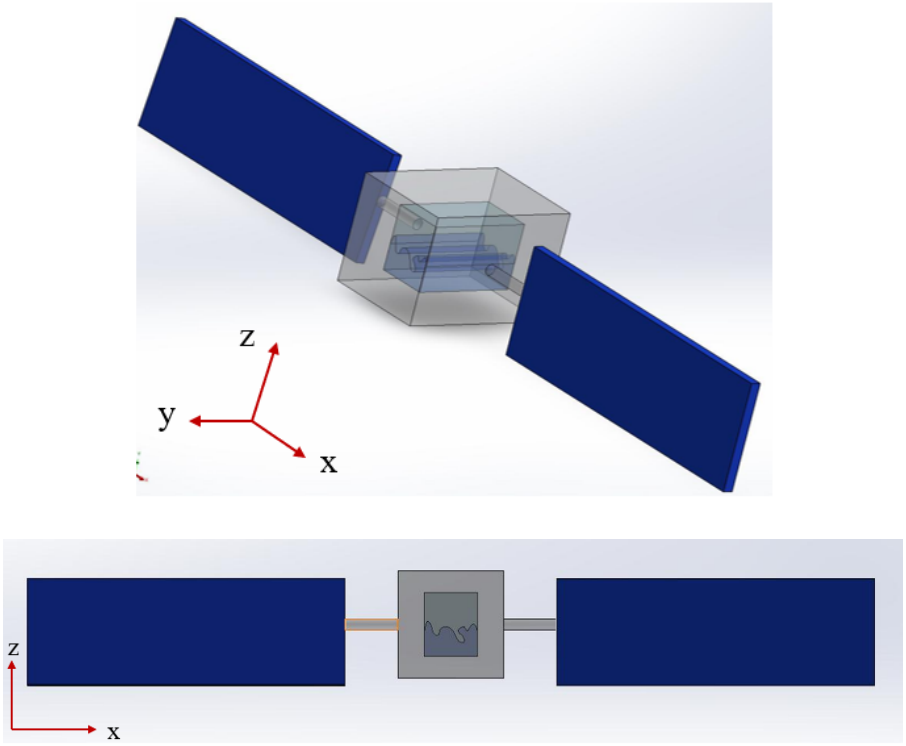

Figure 4: Simplified CAD used to model the satellite.

5.4 Tank geometries

Spherical and cylindrical tanks are commonly used in spacecrafts. Spherical tanks offer uniform stress distribution and minimal surface area, which reduces structural mass, but they are often difficult to integrate into the spacecraft layout.

Cylindrical tanks are widely used because they are easier to manufacture and integrate. They may also include hemispherical or ellipsoidal end caps to reduce stress concentrations and improve structural performance.

Tank geometry has a strong influence on sloshing dynamics. In this study, we simplify the analysis by considering two cases: a cylindrical tank with flat end caps and a rectangular tank. This reduces both analytical and numerical complexity, and the rectangular geometry can be further simplified to a two-dimensional representation.

For both configurations, the total tank volume is taken to be 20 L.

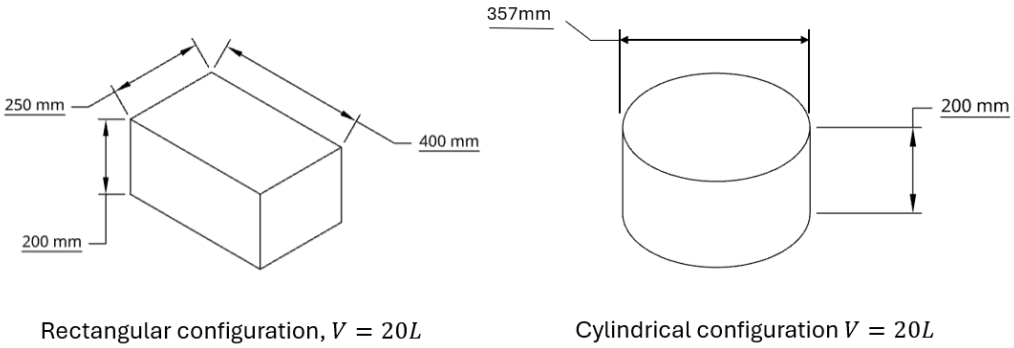

Figure 5: Schematic of the tank geometries considered: cylindrical with flat caps and rectangular.

5.5 Maneuvers Studied and Acceleration Profiles

For this study, we focus on two simplified maneuvers. For convenience in later work, both maneuvers last 50 seconds. While this duration is shorter than real maneuvers, which can last several hours, the chosen accelerations are designed to preserve the main non-dimensional numbers of the problem (the Bond and Weber numbers; Modeling section). This ensures dynamic similarity between the simplified and real maneuvers (Π theorem).

- **Reorientation Maneuver:** This maneuver changes the orientation of the satellite by 10° along its y axis. Such a maneuver could be used to point sensors at a specific area of the sky or Earth.

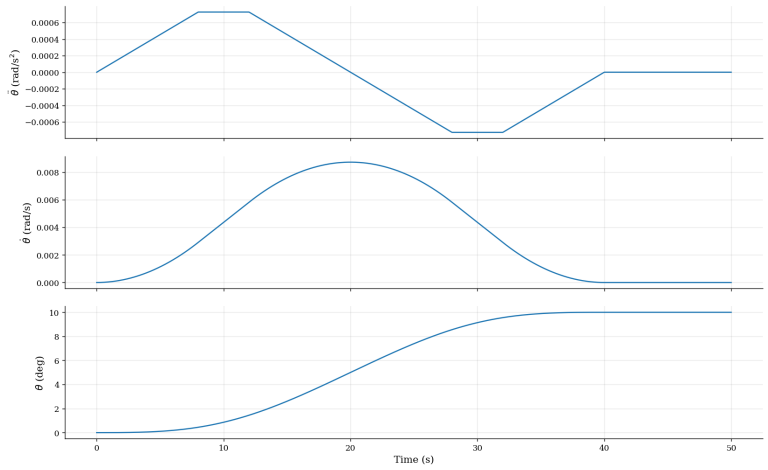

Figure 6: Angular acceleration, velocity, and position for the reorientation maneuver. The maximum angular acceleration is: 7.2×10^{-4} rad/s^2 which corresponds to a maximum tangential acceleration of 2.8×10^{-4} m/s^2.

- **Translation Maneuver:** This maneuver adjusts the satellite's position, targeting a small adjustement in the x diretion (1m). Such burns are typically used to allow position hold or formation flight within a constellation of satellites.

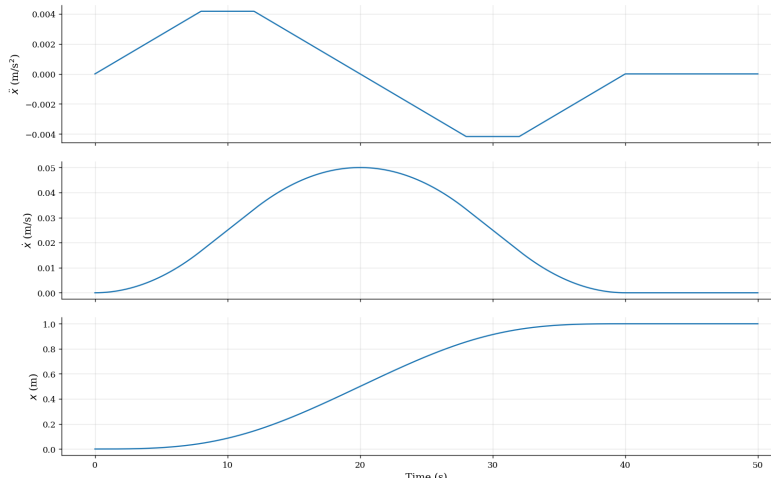

Figure 7: Acceleration, velocity, and position for the orbit correction burn. The maximum acceleration during this maneuver is : 4.2×10^{-3} m/s^2.

Note that both maneuvers are highly simplified compared to real spacecraft operations. However, the study presented in the rest of this paper can be replicated for any kind of acceleration profile.

6 Modeling sloshing in microgravity

With the system parameters and assumptions defined, we now develop analytical models to describe sloshing behavior in microgravity. They provide a first estimate of the dynamics of sloshing, and serve as a basis for interpreting and validating the results from numerical simulations.

6.1 Dimensional Analysis

A liquid–gas system may be governed by inertia, viscous, gravitational, and capillary forces. To identify the dominant effects in microgravity conditions, relevant dimensionless numbers are introduced:

- The Weber number compares inertial forces and capillary force : $We = \frac{\rho v^2 L}{\sigma}$
- The Bond number comparing gravity (body forces) to capillary forces : $Bo = \frac{\rho g L^2}{\sigma}$

Depending on the values of these numbers the flow regime may change.

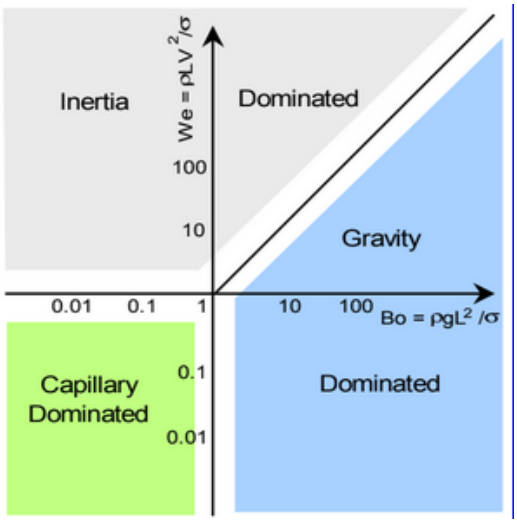

Figure 8: Flow regimes depending on the Bond and Weber numbers.[12]

During spacecraft maneuvers, these dimensionless numbers evolve in time due to changing effective accelerations, which alters the dominant balance of forces and, consequently, the sloshing regime.

The resulting regimes are summarized in the table below:

Dimensionless Number	**Reorientation Maneuver**		**Translation Maneuver**	
	During burn	**After burn**	**During burn**	**After burn**
Weber number (We)	0.6	0.6	544.9	544.9
Bond number (Bo)	6.3	0	181.6	0
Regime	Gravity-dominated	Capillary-dominated	Inertia dominated	Inertia dominated

The results confirm that the flow regime strongly depends on the maneuver type: low-acceleration phases are gravity- or capillary-dominated, whereas high-thrust phases are inertia-dominated. This will be useful to simplify models and simulations.

6.2 Rigid-body approximation for first-order sloshing forces

The simplest sloshing model treats the liquid as a rigid body attached to the tank, with no internal motion. The force is then :

$$\mathbf{F}_{\text{sloshing}}(t) = -m_{Xe}\,\mathbf{a}_{\text{maneuver}}(t)$$

where m_{Xe} is the propellant mass and $\mathbf{a}_{\text{maneuver}}$ the spacecraft acceleration.

The moment is:

$$\mathbf{M}_{\text{sloshing}}(t) = \mathbf{r}_{\text{tank}} \times \mathbf{F}_{\text{sloshing}}(t)$$

with $\mathbf{r}_{\text{tank}}$ the vector from spacecraft to tank center.

This model neglects fluid dynamics, oscillations, phase lag, and center of mass shifts, but provides a first-order upper bound of maneuver-induced loads. For a rectangular tank with part 4 assumptions: $F_{max} = 0.5\,\text{N}$, $M_{max} = 0.09\,\text{N·m}$.

6.3 Small displacements analysis

We consider small-amplitude sloshing under the following assumptions:

- The fluid is incompressible and inviscid.
- The flow is irrotational, such that a velocity potential ϕ exists with $\mathbf{u} = \nabla\phi$.
- The liquid–gas interface is initially flat (contact angle of 90°).
- Interface displacements are small, allowing linearization.

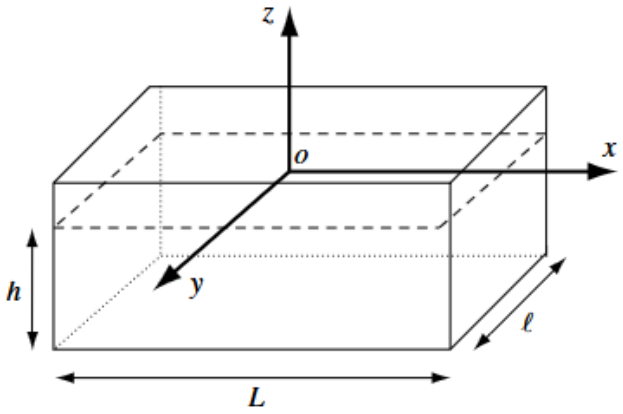

Figure 9: Rectangular tank diagram

Under these assumptions, the flow is governed by Laplace's equation:

$$\nabla^2\phi = 0$$

Boundary conditions are defined as follows:

- No normal flow at the rigid walls:

$$\frac{\partial\phi}{\partial n} = \mathbf{V}_{wall} \cdot \mathbf{n}$$

- Kinematic condition at the free surface (η is the interface displacement):

$$\frac{\partial \eta}{\partial t} = \frac{\partial \phi}{\partial z} \quad \text{at } z = 0$$

- Dynamic condition (linearized Bernoulli equation, assuming small deformations of the interface):

$$\frac{\partial \phi}{\partial t} + g\eta - \frac{\sigma}{\rho}\nabla^2 \eta = 0 \quad \text{at } z = 0$$

Rectangular Tank

For a rectangular tank of length L, height H and liquid depth h, we expand the velocity potential as a sum of orthogonal modes:

$$\phi(x, z, t) = \sum_{n=1}^{\infty} q_n(t) \frac{\cosh k_n(z + h)}{\cosh k_n h} \cos(k_n x), \qquad k_n = \frac{n\pi}{L}.$$

The corresponding free-surface displacement is

$$\eta(x, t) = \sum_{n=1}^{\infty} q_n(t) \cos(k_n x).$$

Substituting these expansions into the boundary conditions gives a set of decoupled **modal equations**:

$$\ddot{q}_n + \omega_n^2 q_n = f_n(t),$$

where $f_n(t)$ represents external forcing (e.g., spacecraft acceleration).

The **natural frequencies** are

$$\omega_n^2 = \left(g k_n + \frac{\sigma}{\rho} k_n^3 \right) \tanh(k_n h),$$

which reduces in microgravity ($g \to 0$) to

$$\omega_n^2 = \frac{\sigma}{\rho} k_n^3 \tanh(k_n h).$$

Cylindrical Tank

For cylindrical tanks with radius R, radial symmetry leads to solutions in Bessel functions:

$$\phi(r,\theta,z,t) = \sum_{m,n} A_{mn}(t) J_m(k_{mn} r)\cos(m\theta)\frac{\cosh(k_{mn}(z+h))}{\cosh(k_{mn}h)}, \quad J'_m(k_{mn}R) = 0,$$

with natural frequencies

$$\omega_{mn}^2 = \left(g k_{mn} + \frac{\sigma}{\rho} k_{mn}^3\right) \tanh(k_{mn}h),$$

reducing in microgravity to

$$\omega_{mn}^2 = \frac{\sigma}{\rho} k_{mn}^3 \tanh(k_{mn}h).$$

Modes are indexed by radial and azimuthal numbers (n, m).

6.3.1 Mechanical models

To enable efficient simulation of sloshing dynamics, the continuous fluid system is approximated by a finite set of coupled oscillators. The parameters of the model come from the earlier linear developments.

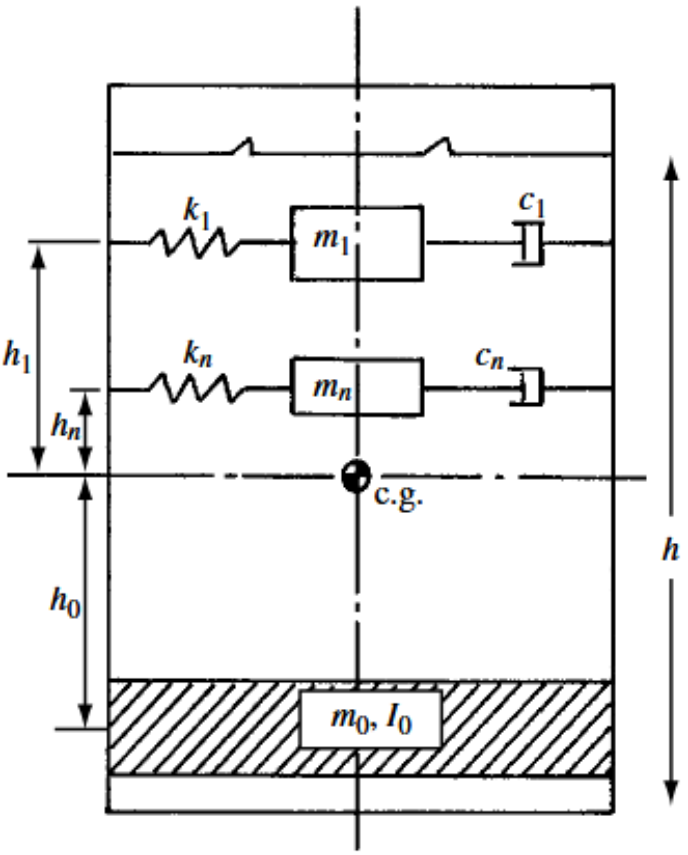

Figure 10: Equivalent mechanical model for sloshing. Image taken from [n]. A fixed mass m_0 is considered as well as n modal masses and heights m_n, h_n

Let's consider that the n first modes participate significantly. We must have :

Mass conservation

$$m_{tot} = m_0 + \sum_{i=1}^{n} m_i$$

Inertia conservation

$$I = I_0 + m_0 h_0^2 + \sum_{i=1}^{n} m_i h_i^2$$

The spring constants can be deduced from the natural circular frequencies derived :

$$K_n = \omega_n^2 m_n$$

It is possible to derive the properties (m_n,h_n) through tedious calculations that can be found in R. A. Ibrahim's book [12]. Properties vary with the shape of the tank considered. Damping can not be analytically derived since we assumed an inviscid fluid, it will be ignored for the time being and computed through numerical simulations later.

The problem can then be re-expressed in the condensed form:

$$\mathbf{M}\,\ddot{\mathbf{q}}(t) + \mathbf{C}\,\dot{\mathbf{q}}(t) + \mathbf{K}\,\mathbf{q}(t) = \mathbf{F}(t) \tag{5}$$

where the generalized coordinate vector is:

$$\mathbf{q} = \begin{bmatrix} x & \psi & x_1 & \cdots & x_n \end{bmatrix}^T \tag{6}$$

with x being the displacement of the tank and ψ being the rotation of the tank with respect to its center of mass. x_n refer to the horizontal position of mass m_n.

Mass matrix

$$\mathbf{M} = \begin{bmatrix} m_0 + \sum_{i=1}^{n} m_i & -m_0 h_0 + \sum_{i=1}^{n} m_i h_i & m_1 & \cdots & m_n \\ m_0 h_0 + \sum_{i=1}^{n} m_i h_i & I_0 + m_0 h_0^2 + \sum_{i=1}^{n} m_i h_i^2 & m_1 h_1 & \cdots & m_n h_n \\ m_1 & m_1 h_1 & m_1 & & 0 \\ \vdots & \vdots & & \ddots & \\ m_n & m_n h_n & 0 & & m_n \end{bmatrix} \tag{7}$$

Damping matrix

$$\mathbf{C} = \begin{bmatrix} 0 & 0 & 0 & & \\ 0 & 0 & 0 & & \\ 0 & 0 & 2m_1\omega_1\zeta_1 & & 0 \\ \vdots & \vdots & & \ddots & \\ 0 & 0 & 0 & & 2m_n\omega_n\zeta_n \end{bmatrix} \tag{8}$$

Stiffness matrix

$$\mathbf{K} = \begin{bmatrix} 0 & 0 & 0 & \cdots & 0 \\ 0 & 0 & 0 & \cdots & 0 \\ 0 & 0 & K_1 & \cdots & 0 \\ \vdots & \vdots & \ddots & & \\ 0 & 0 & \cdots & K_n & \end{bmatrix} \tag{9}$$

Sloshing effects

$$\mathbf{F}(t) = \begin{bmatrix} -F_x(t) \\ M_y(t) \\ 0 \\ \vdots \\ 0 \end{bmatrix} \tag{10}$$

where F_x is the sloshing force along x and M_y is the moment due to sloshing.

Center of mass displacement in the tank frame The center of mass of the liquid-sloshing system relative to the tank is given by:

$$x_{\text{CM,tank}} = \frac{\sum_{i=1}^{n} m_i x_i}{m_0 + \sum_{i=1}^{n} m_i} = \frac{\mathbf{m}^T \mathbf{x}_s}{m_{\text{tot}}} \tag{11}$$

where $\mathbf{x}_s = [x_1, x_2, \ldots, x_n]^T$ is the vector of sloshing displacements of the liquid masses relative to the tank, $\mathbf{m} = [m_1, m_2, \ldots, m_n]^T$ is the vector of sloshing modal masses, and $m_{\text{tot}} = m_0 + \sum_{i=1}^{n} m_i$ is the total mass of the system including the tank.

Simulation This system is simulated in Python by solving differential equations to compute force, moment, and center of mass displacement. Parameters are calculated separately and fed into the model.

Since the response may be linear or nonlinear depending on the maneuver, results should be interpreted cautiously and validated with CFD.

Results are shown for a rectangular tank (2D: forces and moments per unit length):

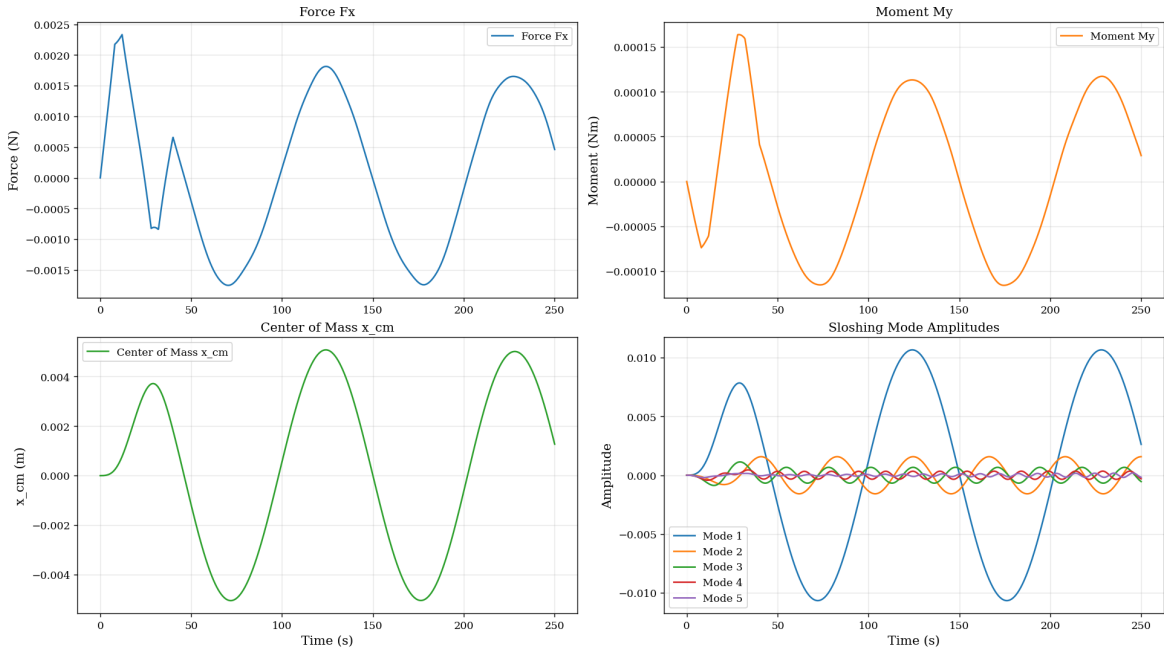

Figure 11: Mechanical model force, moment and center of mass displacement(in the tank's frame) for a reorientation maneuver. A plot of modal displacements is also provided.

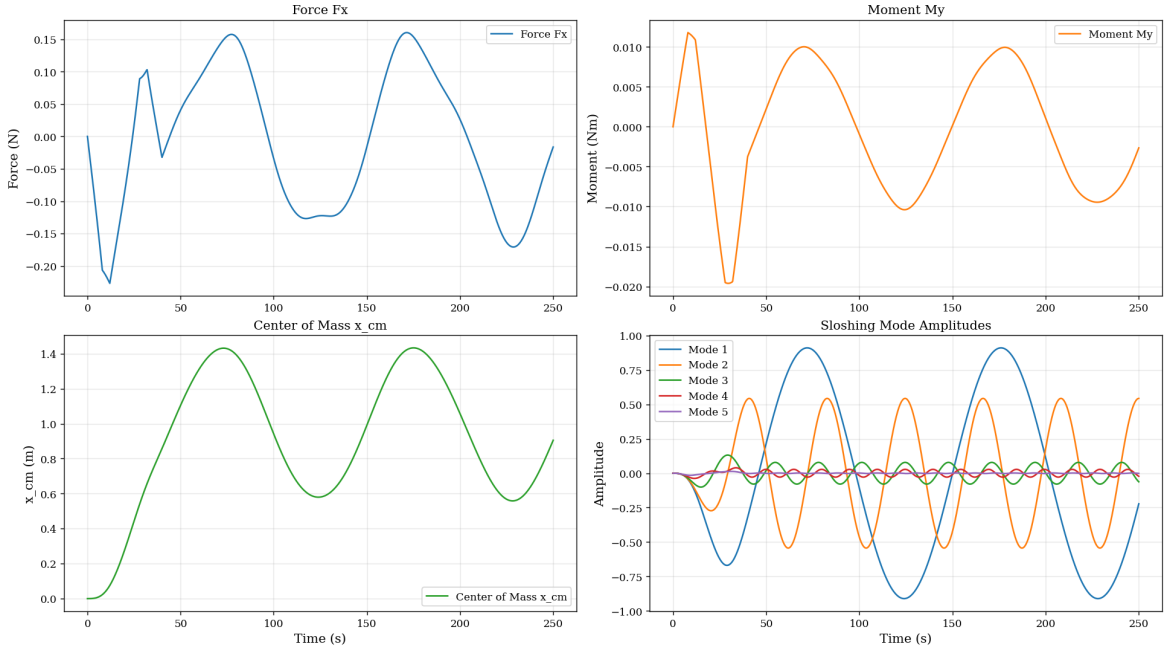

Figure 12: Mechanical model predicted force,moment and center of mass displacement (in the tank's frame) predictions for an orbital correction maneuver.

The results in the case of a cylindrical tank are very similar and will not be presented here. We can notice that the two first modes contribute the most to the overall dynamics of the sloshing (higher amplitudes). Comparing the energy carried by the first two modes to the total energy in the system gives: $\frac{E_{modes1/2}}{E_{tot}} = 0.998$ for the reorientation maneuver and $\frac{E_{modes1/2}}{E_{tot}} = 0.991$ for the orbital adjustment maneuver. This indicates that the first two modes capture more than 99% of the system energy, allowing higher-order modes to be neglected without significant loss of accuracy. While these analytical models provide insight into the underlying physics, numerical

simulations are required to capture nonlinear effects and validate the predictions.

6.4 Non linear sloshing

The mechanical models assume small-amplitude, linear sloshing, but real spacecraft maneuvers can introduce nonlinear fluid effects. Large accelerations or rapid attitude changes may cause interface deformation and bubble formation, which are not captured by linear models.

During rapid maneuvers or thrust cut-off, the liquid surface in a partially filled tank can deform significantly and even break up into bubbles depending on fill level. In microgravity, where surface tension dominates, the fluid may form clusters, wall films, or liquid bridges instead of a single free surface. These large displacements and curvatures of the interface effectively make the linearization of the equations impossible, breaking the model.

Non linear sloshing is often using descriptive models that fit parameters to a standard model to match numerical simulations and experiments.

A full nonlinear model is beyond this work's scope as it demands large datasets, but CFD simulations will be used on selected cases to evaluate these effects against linear results and understand where the limit between the two regimes is.

7 Simulations and numerical work

This section presents the numerical simulations performed in this study. They are used to validate the analytical models, assess their limits, and generate data to estimate attitude disturbances induced by sloshing.

7.1 Solvers and method used

The simulations were carried out using ANSYS Fluent and Simscale multiphase fluid solver.

Simulations were performed using ANSYS Fluent and Simscale multiphase solvers. Sloshing is modeled as a two-phase (liquid–vapor) flow using the Volume of Fluid (VOF) method. This approach tracks the phase distribution through a volume fraction field ranging from 0 (gas) to 1 (liquid), which is advected alongside the Navier–Stokes equations. Surface tension was applied for the capillary dominated sections of the maneuvers (see part 5 for the Bond and Weber numbers explanations).

For this method a necessary condition for convergence is maintaining the global Courant number $Co = U\frac{\Delta t}{\Delta x}$ inferior to 0.5 (recommended value). Where U is the velocity of the fluid, Δx is the mesh size and Δt is the time step. We choose a limit of 0.4 for safety. This constraint, combined with the mesh resolution, requires small time steps and leads to high computational cost.

The imposed acceleration (maneuver excitation) is modeled using a moving mesh, ensuring consistent coupling between tank motion and fluid response.

We consider a simulation to be a success if all the residuals (numerical errors) stay under 10^{-4}.

7.2 2D rectangular tank case

For 2D simulations an very important assumption is made : it is possible to extend 2D results to 3D results because of invariance in the direction normal to sloshing (quantities are per unit length and multiplying them by the width of the tank gives 3D results). This assumption holds because the rectangular geometry is uniform. However it becomes less and less accurate as we get closer to the walls notably due to viscosity effects.

The simulations performed have the following objectives:

- (1) Validation of linear model predictions via modal frequency extraction.
- (2) Investigation of nonlinear behavior at high accelerations
- (3) Reorientation maneuver simulation
- (4) Orbital correction maneuver simulation

7.2.1 Setup of the simulations

An adaptive mesh refinement strategy is used, refining the mesh near the liquid–vapor interface every two time steps.

Fluid properties and tank geometry are defined in Section 4. In the absence of detailed data, a contact angle of $\pi/2$ is assumed. Boundary conditions are taken to be non slip at the walls. Unless specified otherwise initial interfaces are flat.

Figure 13: Mesh used for the simulations. The mesh is shown at t=0 and t=10s. The size of the mesh was chosen after comparing results for different mesh sizes until result variation was negligible.

The specificity of each simulation is detailed below :

- For (1) we have

$$a_{\text{input}}(t) = \begin{cases} 0.0005\,\text{m/s}^2, & 0 \leq t \leq T_i \\ 0, & t > T_i \end{cases}$$

  A step acceleration is applied to let the system evolve freely and extract modal frequencies. Five equally spaced probes are placed along the liquid–vapor interface to track the time evolution of the interface height. The initial interface is flat.

- For (2) : The accelerations used are sinusoidal :$a(t) = A\cos(2\pi ft)$ with amplitude A and the frequency f being fixed at 1.5 Hz.

- For (3) and (4) we use the profiles provided in part 4.

7.2.2 Simulation (1)

The first simulation is meant to compute modal frequencies by tracking the interface height at different locations.

The system is behaving linearly in this case as the interface displacement varies by a few percent (15% at most) throughout the simulation.

According to the linear modeling performed previously we should have for a rectangular tank:

$$\eta(t,x) = \sum_{n=1}^{\infty} q_n(t)\, \cos(k_n x) \tag{12}$$

$$q_n(t) \approx A_n \cos(\omega_n t + \phi_n) \tag{13}$$

$$\hat{\eta}(\omega,x) = \sum_{n=1}^{\infty} \cos(k_n x) \int_0^T A_n \cos(\omega_n t + \phi_n)\, e^{-i\omega t}\, dt \tag{14}$$

Peaks of $\hat{\eta}(\omega,x)$ thus occur at $\omega = \omega_n$ revealing modal frequencies.

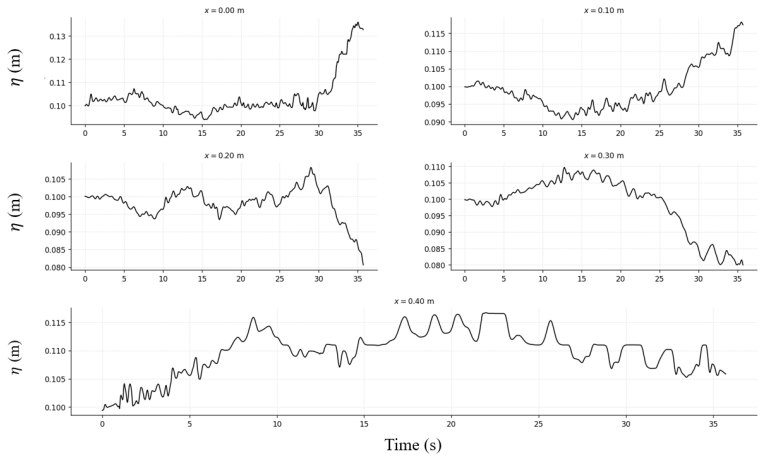

Figure 14: Elevation of the interface in the frame of the tank at 5 different probes distributed along the tank's length. The signals are filtered to get rid of numerical noise.

Based on those results a Fast Fourier Transform can be performed to get the main frequencies of the signal.

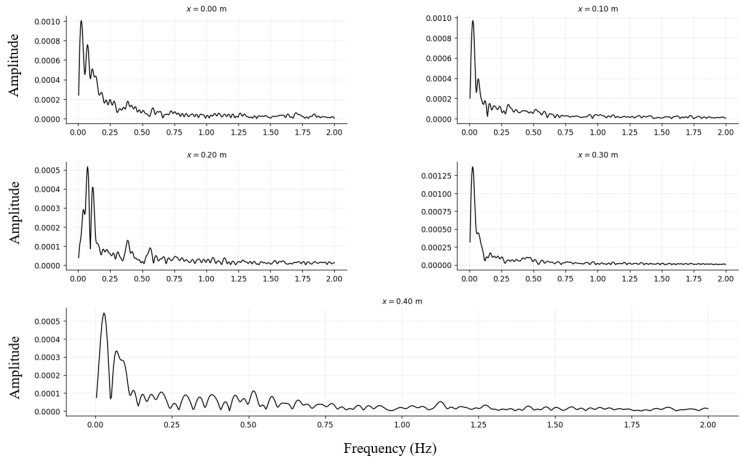

Figure 15: Fast Fourier Transform of each of the elevation heights recorded during the simulation. The dominant frequencies correspond to the highest peaks, all the signals seem to share the same first frequencies.

We can now compare the theoretical frequencies and the one obtained with CFD.

Mode Number	**Linear Model frequency (rad/s)**	**CFD frequency (rad/s)**	**Relative error (%)**
1	0.07	0.072	2.86
2	0.19	0.2	5
3	0.35	0.36	2.86
4	0.50	0.58	16
5	0.75	0.82	9.33

Table 1: Comparison of theoretical and CFD calculated modal frequencies. For each mode, the CFD value is obtained by taking the average value of the frequencies corresponding to that mode from the 5 FFT profiles computed previously.

The results match closely the expected values for the first three modes. Errors tend to become more noticeable for higher modes probably because of the complex effects induced by the vapor flow. However since only the two first modes contribute meaningfully to the sloshing we can consider that the model works well (within 5%) to predict results in the linear sloshing domain.

This first set of simulations verified the results from the linear model by comparing obtained modal frequencies. It gives us confidence in the accuracy of our previous linear sloshing model.

7.2.3 Simulation (2)

Having validated the linear model, we now investigate the limits of its applicability by exploring nonlinear behavior.

The first simulation of this set aims at capturing the transition between linear and non-linear behavior as a function of input acceleration.

A range of sinusoidal acceleration profiles are applied with varying amplitudes (A). The initial interface is flat and the fill fraction is taken to be 0.5.

We have to define an empirical way to set a limit between linear and non-linear behavior. As we know that non nonlinearities happen when interface displacement becomes significant, we have made the following choice:

$$\gamma = \frac{\max|\eta(x,t)|}{H} \tag{15}$$

A threshold value η_c is arbitrarily introduced to distinguish between regimes:

$$\gamma \leq \gamma_c \;\Rightarrow\; \text{linear regime}, \qquad \gamma > \gamma_c \;\Rightarrow\; \text{non-linear regime}. \tag{16}$$

To identify the threshold γ_c we look at the performance of the model when trying to match outputs. We look at the force predicted by the model against the one from the simulation. We define an maximum error for the model to be considered applicable : $\text{NRMSE} = \frac{\|F_{\text{CFD}} - F_{\text{model}}\|_2}{\|F_{\text{CFD}} - \bar{F}_{\text{CFD}}\|_2} = 15\%$. If that limit is exceeded the regime is non linear.

$\gamma_c = 0.3$ is finally adopted.

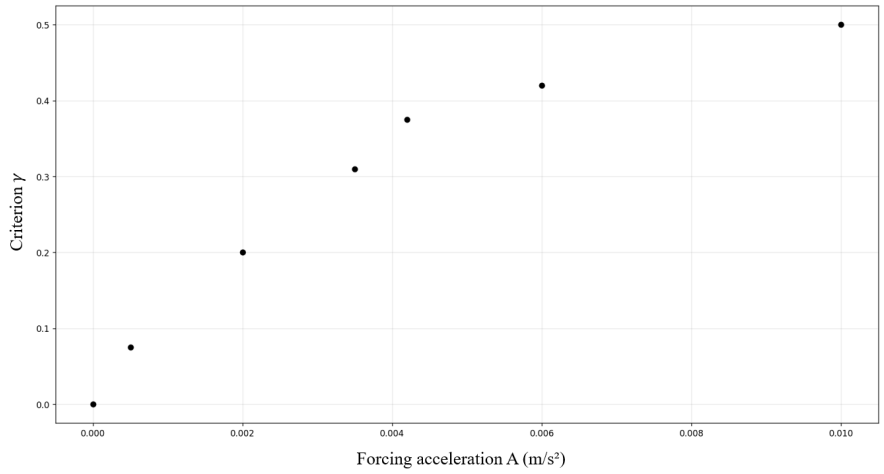

Figure 16: Plot of γ as a function of the forcing amplitude A. The maximum possible value of γ is 0.5, corresponding to a full displacement of the interface from mid-height.

From the plot we extrapolate that the transition between linear and non linear regimes happens somewhere between accelerations of 0.003 m/s^2 and 0.0035 m/s^2. This study is limited since we haven't assessed the impact of frequency but provides a first idea of the limit to the validity of linear models.

7.2.4 Simulation (3) and (4)

The cases simulated correspond to the original maneuvers described in part 4. We will compare the results with the models and fit the values of damping from the mechanical model using a least square algorithm. Since the accelerations are below the limit established previously the responses should be linear and the model should hold.

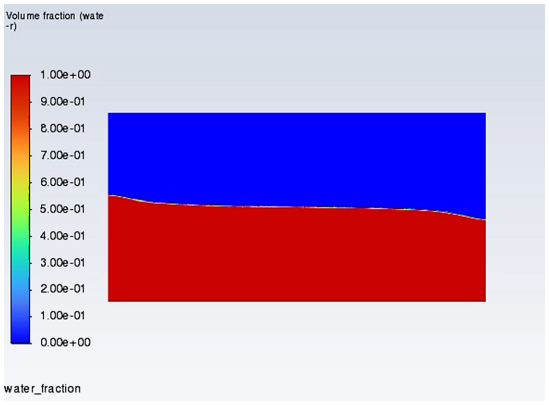

Figure 17: Volume fraction (red is liquid, blue is vapor) for $A = 0.002m/s$ at t=8s when the maximum value for *eta* is reached for the first time. This case is linear with small displacements.

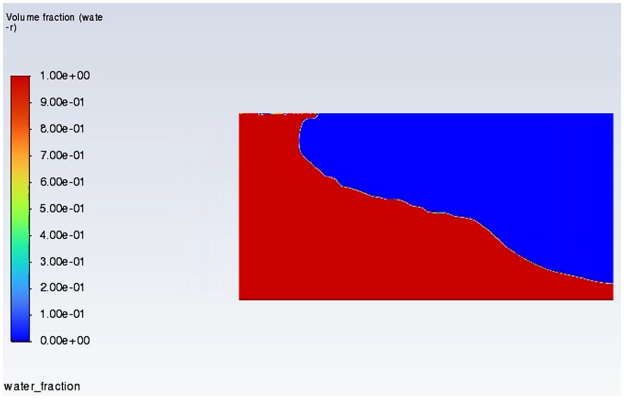

Figure 18: Volume fraction for $A = 0.01m/s$ at t=12 s. We can clearly identify nonlinearities with the beginning of a wave break and large displacements.

To quantify model performance we compute the normalized root mean squared error. For example for the force :

$$\text{NRMSE} = \frac{\|F_{\text{CFD}} - F_{\text{model}}\|_2}{\|F_{\text{CFD}} - \bar{F}_{\text{CFD}}\|_2}$$

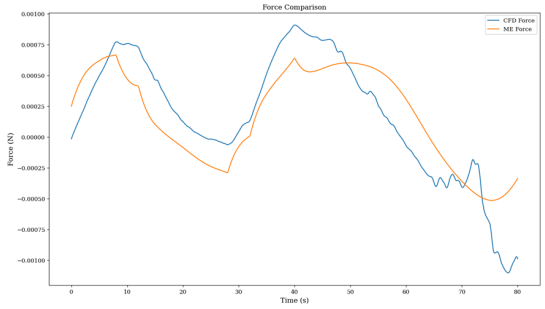

(a) CFD vs mechanical force. NRMSE 14%

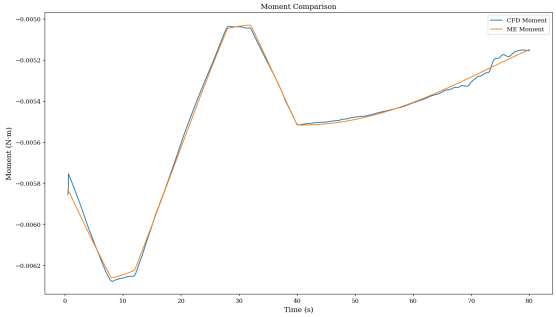

(b) CFD vs mechanical moment. NRMSE 8%

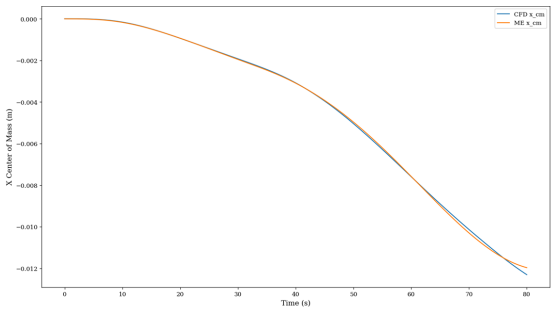

(c) CFD vs mechanical center of mass displacement. NRMSE 1%

Figure 19: Comparison between CFD results and the mechanical model for the reorientation maneuver. Damping coefficients were identified using a least-squares method and applied before comparison. Agreement is good with errors below 15%, and peak amplitudes are well captured. This is expected as the maximum tangential acceleration for this maneuver is 2.8e-4 m/s^2 which is below the acceleration limit we established for non linear sloshing.

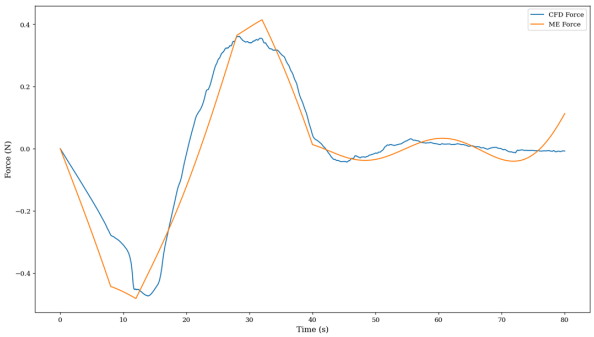

(a) CFD vs mechanical force.NRMSE 17.4%

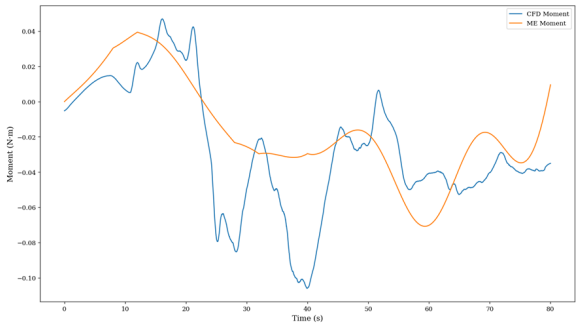

(b) CFD vs mechanical moment.NRMSE 24%

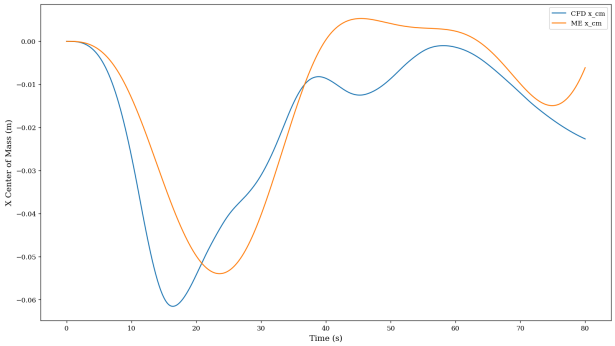

(c) CFD vs mechanical center of mass displacement. NRMSE 10.8%

Figure 20: Results of the simulations compared with the mechanical model for the orbital correction maneuver. Damping coefficients were obtained using a least-squares method and applied before comparison. The model results are shown in orange and simulations in blue. The model provides a poor prediction of the dynamics with large errors being observed. This is once again expected as the maximum acceleration for this maneuver exceeds the limit established before.

These results confirm that the mechanical model provides reliable estimates for low-acceleration, near-linear sloshing conditions. However is breaks down significantly once the non linear regime is reached. The CFD data obtained here will be used for attitude analysis later.

7.3 3D cylindrical tank case

For the 3D simulations of the cylindrical geometry we choose to switch software and use Simscale for meshing and computation power reasons (cloud based software).

Due to a lack of time only early results have been obtained. Simulations should be completed in the relevant cases in the future.

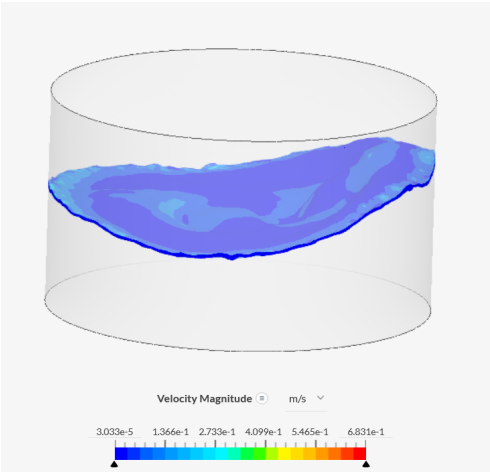

(a) Velocity magnitude on the interface at t=8s (maximum displacement time)

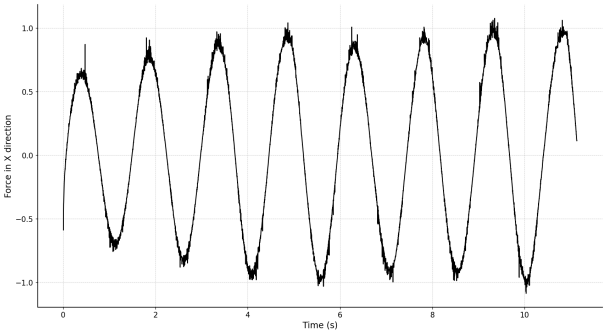

(b) Force in x direction as a function of time.

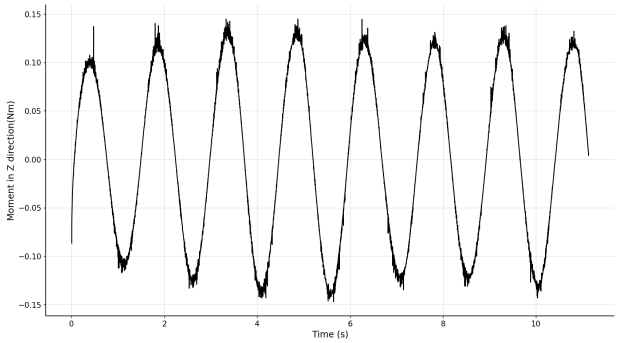

(c) Moment in z direction as a function of time.

Figure 21: Results of 3D simulation for a sinusoidal acceleration along x of amplitude 0.0005 m/s^2 and frequency 0.7 Hz.

The numerical simulations performed in this section validate the mechanical model and linear theory, while also identifying the limits of the linear sloshing assumption and characterizing bubble-driven nonlinear behavior. The resulting data will be used in subsequent attitude dynamics analysis.

8 Effects on satellite attitude

The high-fidelity CFD analysis yielded the foundational data for this study, specifically the sloshing force, sloshing moment, and the transient drift of the Xenon center of mass. To assess the resulting impact on spacecraft stability, a rigid body dynamics analysis was developed utilizing the 6DOF (Six Degrees of Freedom) solver within MATLAB/Simulink. This tool integrates the translational and rotational equations of motion, allowing for a coupled simulation of the fluid-structure interaction.

The 6DOF analysis provides a comprehensive assessment of the satellite's state, including its attitude, position, angular velocity, and translational velocity. Furthermore, to ensure the sloshing effects remain within controllable limits, the simulation determines the required control torque, accumulated angular momentum, and linear momentum. These values are essential for

verifying that the disturbances do not exceed the operational design specifications of the ARW-1A reaction wheel.

While the force ($\mathbf{F}_{CFD}$) and moment ($\mathbf{M}_{CFD}$) were obtained from a 2D analysis, due to geometry of the propellant tank being assumed to be a rectangular prism, similarity can be assumed along the third dimension. Consequently, all 2D parameters are multiplied by the effective width of the tank to extrapolate the results into a 3D context. Given these inputs, the dynamics are defined as follows:

a. Translational Dynamics

The acceleration of the satellite in the inertial frame is determined by Newton's Second Law:

$$\mathbf{a} = \frac{1}{m}\mathbf{F}_{CFD} \tag{17}$$

$$\mathbf{v} = \mathbf{v}_0 + \int_0^t \mathbf{a}\ dt \tag{18}$$

$$\mathbf{s} = \mathbf{s}_0 + \int_0^t \mathbf{v}\ dt \tag{19}$$

m is the total mass of the satellite. The solver then integrates $\mathbf{a}$ to solve for the velocity $\mathbf{v}$ and the position $\mathbf{r}$ using the "ode45" solver.

b. Rotational Dynamics

The attitude of the satellite is governed by Euler's equations for a rigid body. The relationship between the CFD-induced moment and the angular velocity $\boldsymbol{\omega}$ is:

$$\mathbf{M}_{CFD} = \mathbf{I}\dot{\boldsymbol{\omega}} + \boldsymbol{\omega} \times (\mathbf{I}\boldsymbol{\omega}) \tag{20}$$

To solve for the angular acceleration $\dot{\boldsymbol{\omega}}$, the equation is rearranged:

$$\dot{\boldsymbol{\omega}} = \mathbf{I}^{-1}\left[\mathbf{M}_{CFD} - \boldsymbol{\omega} \times (\mathbf{I}\boldsymbol{\omega})\right] \tag{21}$$

where $\mathbf{I}$ represents the time-varying inertia matrix of the satellite, accounting for the center of mass drift of the Xenon. The angular rate is then solved for using the "ode45" solver as well.

c. Kinematic Transformation

The angular rates in the body frame are converted to Euler angle rates $(\dot{\phi}, \dot{\theta}, \dot{\psi})$ to find the satellite's angular orientation:

$$\begin{bmatrix} \dot{\phi} \\ \dot{\theta} \\ \dot{\psi} \end{bmatrix} = \begin{bmatrix} 1 & \sin\phi \tan\theta & \cos\phi \tan\theta \\ 0 & \cos\phi & -\sin\phi \\ 0 & \sin\phi \sec\theta & \cos\phi \sec\theta \end{bmatrix} \begin{bmatrix} \omega_x \\ \omega_y \\ \omega_z \end{bmatrix} \tag{22}$$

$$\psi = \psi_0 + \int_0^t \dot{\psi}\, dt \tag{23}$$

8.1 Preliminary Results

Using the Rigid Body Dynamics solver, a spatial and attitude response was determined, yielding the satellite's location, linear velocity, attitude, and angular velocity. This analysis was conducted for both the reorientation maneuver and the orbit correction burn. The attitude and spatial effects are presented in the figures below.

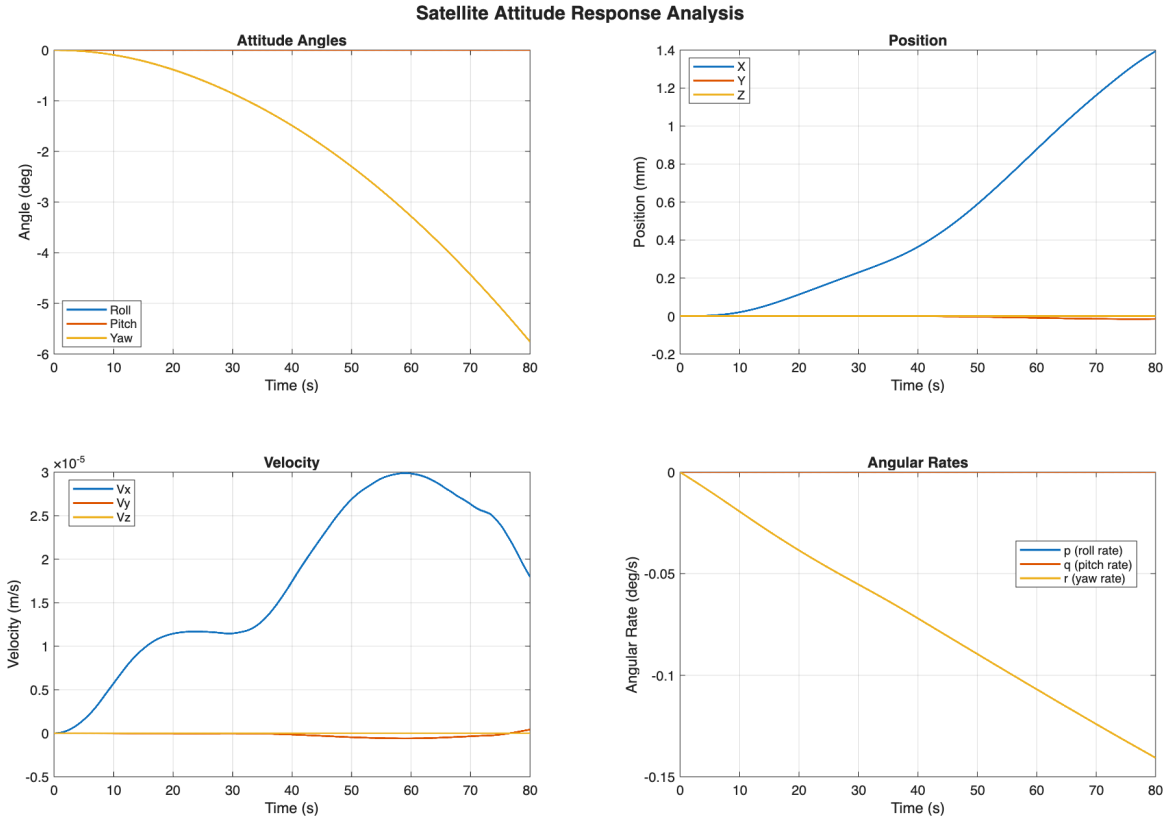

Figure 22: Reorientation Maneuver 6DOF response

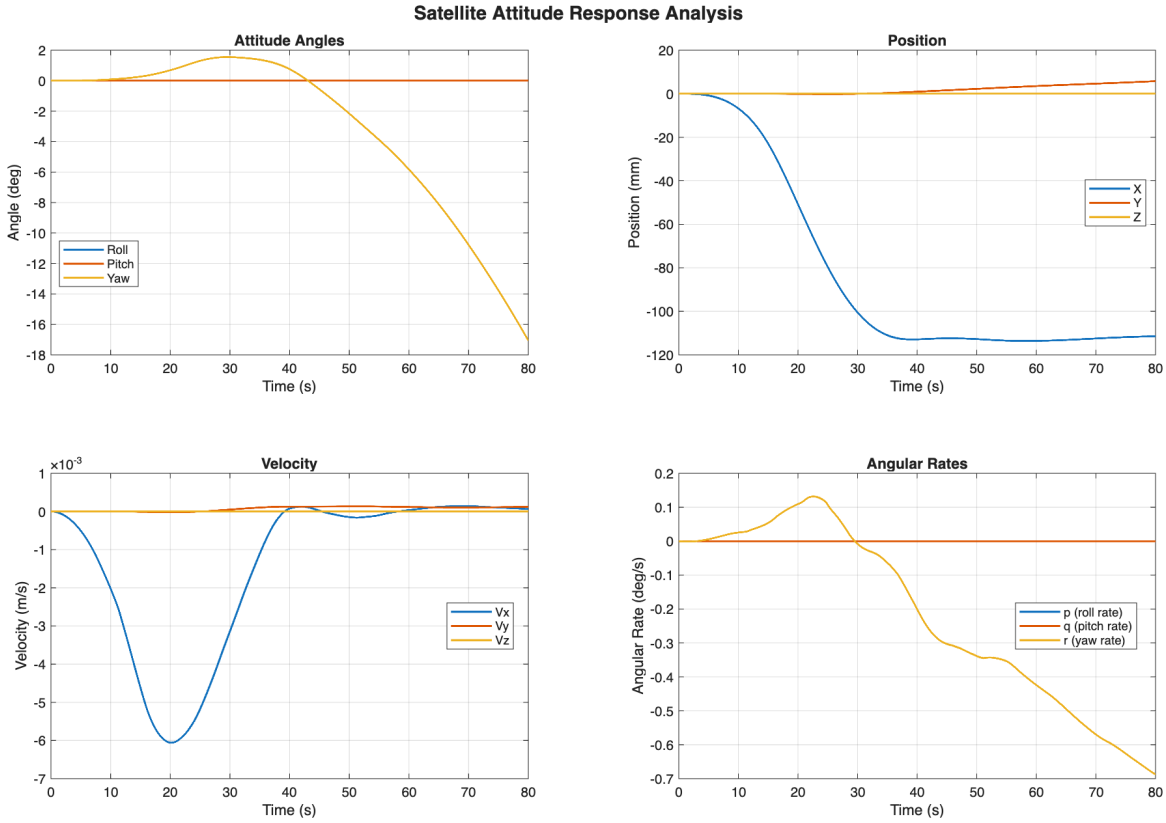

Figure 23: Translational maneuver 6DOF response

8.2 Torque and Linear Momentum

In order to properly understand the magnitude of the attitude effects, it is important to look at the satellite's torque and momentum effects. These values are essential, when looking at the capabilities of the satellite's reaction wheels. Having a torque or total torque that is too high can lead to the satellite's attitude becoming unstable, and thus uncontrollable.

a. Torque and Control Authority

The instantaneous moment $\mathbf{M}_{CFD}$ represents the disturbance torque that the reaction wheels must counteract to maintain a stable attitude. For the purpose of the study, the center of gravity of the propellant tank is assumed to be in the same location as the center of gravity of the satellite. Therefore, the control torque requirement is defined directly by the instantaneous moment from the CFD:

$$\tau = \mathbf{M}_{CFD} \tag{24}$$

b. Momentum Storage and Saturation

The total torque, or accumulated angular momentum $\mathbf{H}_{slosh}$, is the time-integral of the moment. This value determines the "momentum loading" on the wheels:

$$\mathbf{H}_{slosh}(t) = \int_{t_0}^{t} \mathbf{M}_{CFD}(\tau)\, d\tau \tag{25}$$

In Nms, this total torque must remain within the wheel's momentum storage envelope to prevent saturation. A comparison between the peak $\mathbf{H}_{slosh}$ and the wheel capacity is critical to determine if the sloshing leads to a loss of control or requires frequent momentum dumping.

c. Linear Momentum

The translational impact is quantified via the linear momentum $\mathbf{p}$, which accounts for the mass of the propellant and the center of mass drift:

$$\mathbf{p}(t) = m(t)\mathbf{v}(t) = \frac{d}{dt}\mathbf{F}_{CFD} \tag{26}$$

This allows for the assessment of trajectory deviations during orbital correction burns, specifically comparing the momentum distribution between the "Peak" (wet) and "Low" (dry) satellite configurations.

The torque and momentum values are shown in the figures below.

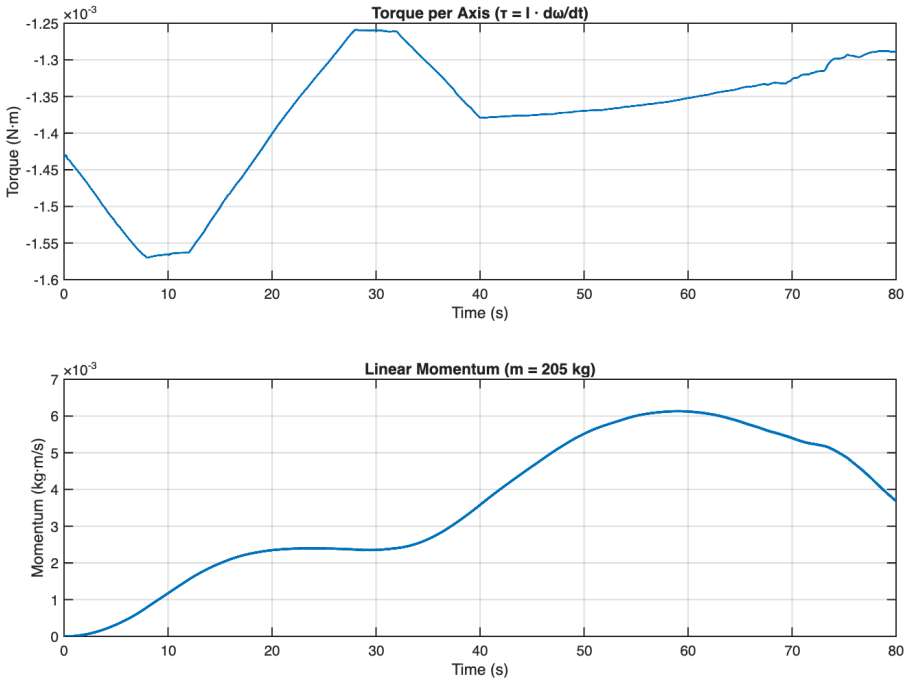

Figure 24: Rotational Maneuver Torque and Momentum Response

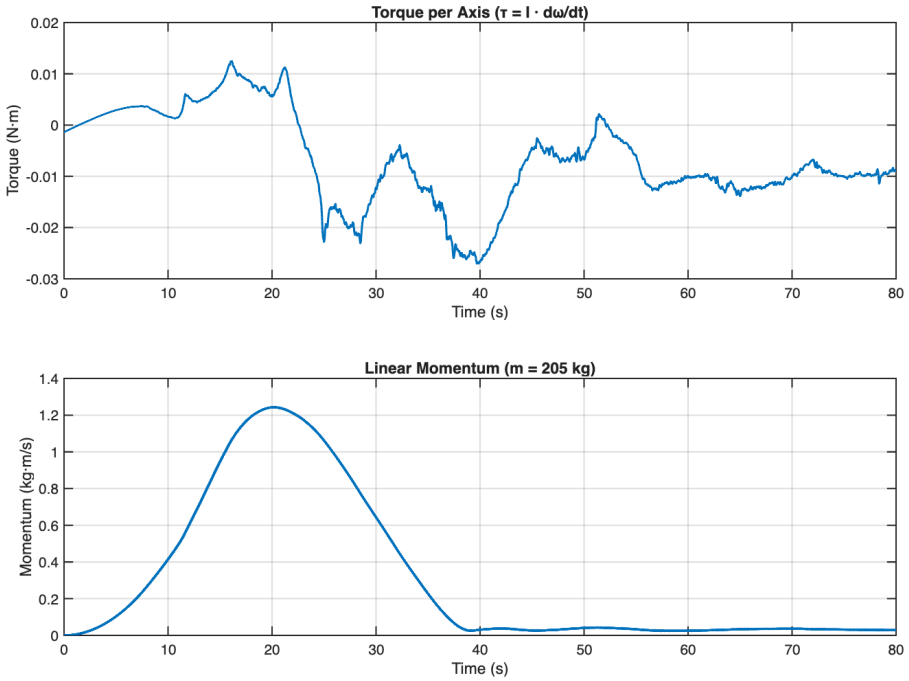

Figure 25: Translational Maneuver Torque and Momentum Response

8.3 Controllability of Sloshing Effects

The 6DOF simulation yielded the peak sloshing values summarized in Table 2. To provide a practical engineering context for these results, the sloshing dynamics were compared directly against the operational limits of the ARW-1A reaction wheel, which is a standard actuator for a 200 kg class satellite.

Table 2: Peak sloshing dynamics compared against ARW-1A reaction wheel engineering limits.

Metric	**Translational Maneuver**	**Rotational Maneuver**	**ARW-1A Limit (200 kg class sat)**
Max Linear Momentum (kg·m/s)	1.2425	0.0061	–
Max Instantaneous Torque (Nm)	0.027049	0.001570	0.1
Max Accumulated Torque (Nms)	0.538547	0.110147	1.0

The analysis reveals that even under peak sloshing conditions during translational maneuvers, the instantaneous torque and the accumulated torque remain significantly below the engineering limits of the wheel. Specifically, the peak torque represents only about 27% of the wheel's 0.1 Nm capacity, and the accumulated torque utilizes approximately 54% of the 1.0 Nms momentum storage. This wide safety margin indicates that the Xenon propellant sloshing is well within the control authority of the satellite's Attitude Control System , ensuring that the sloshing effects are manageable without the risk of actuator saturation or loss of attitude stability.

Furthermore, the peak linear momentum values recorded (1.2425 kg·m/s for the translational case) are found to be negligible in the context of the satellite's orbital dynamics. For a 200

kg class satellite, this momentum transfer results in an extremely small velocity perturbation (approximately 0.006 m/s). This level of deviation is well within the correction capabilities of the propulsion system and does not pose a threat to the station-keeping or orbital accuracy of the mission. Consequently, both the rotational and translational effects of the Xenon sloshing are considered manageable and controllable within the current design parameters.

8.4 Comparative Analysis: Satellite Mass and Inertia

While the magnitude of the sloshing torque and the theoretical controllability of the fluid are independent of the satellite's total mass and inertia, these parameters significantly influence the resulting attitude response. A lower system mass and inertia increase the satellite's sensitivity to sloshing disturbances, leading to higher magnitudes of attitude and positional drift for a given disturbance impulse.

To quantify these effects, two distinct mass profiles are analyzed. The primary profile represents a full-payload configuration with a total mass of 205.112 kg. A second, comparative profile is introduced representing an empty-payload configuration with a mass of 118.496 kg. The corresponding inertia matrices for both configurations are defined as follows:

Inertia With Payload (Total Mass = 205.112 kg)

$$I_{high} = \begin{bmatrix} 36.25 & 0 & 0 \\ 0 & 29.7478 & 0 \\ 0 & 0 & 44.8639 \end{bmatrix} \text{kg} \cdot \text{m}^2 \tag{27}$$

Inertia Without Payload (Total Mass = 118.496 kg)

$$I_{low} = \begin{bmatrix} 25.7389 & 0 & 0 \\ 0 & 16.6069 & 0 \\ 0 & 0 & 30.4959 \end{bmatrix} \text{kg} \cdot \text{m}^2 \tag{28}$$

Using the previously defined mass profiles, the 6DOF analysis is repeated, yielding the following results in Figures 26 and 27. Furthermore, Tables 3 and 4 represent the quantitative summary of the peak and final state deviations, providing a direct comparison of the satellite's dynamic response under different loading conditions.

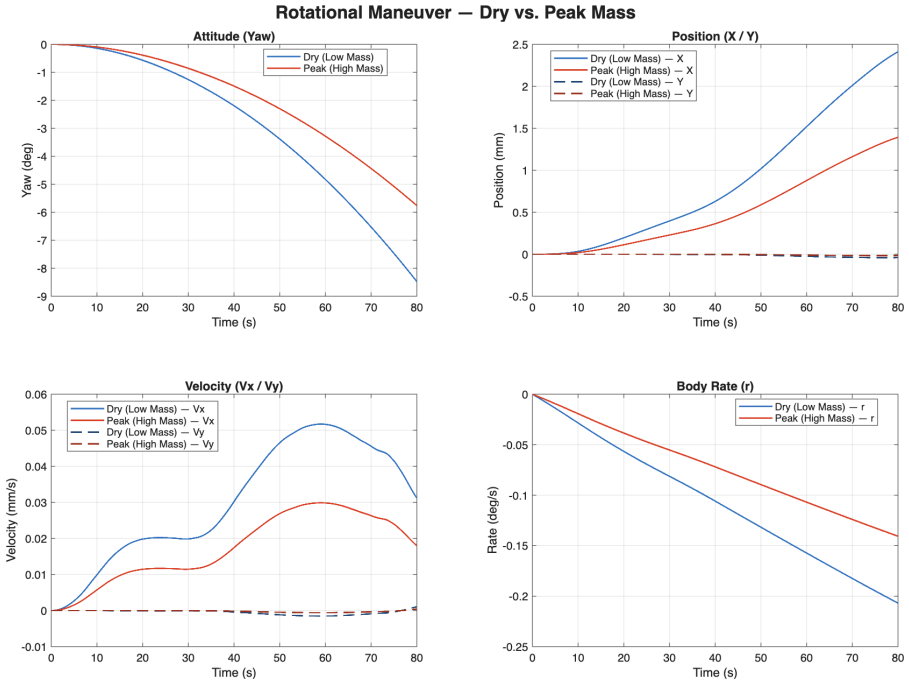

Figure 26: Reorientation Maneuver 6DOF response for Variable Satellite Mass

Table 3: Satellite attitude and positional response during the Reorientation Maneuver.

Metric	**Low Mass (118.5 kg)**	**High Mass (205 kg)**
Final Yaw (deg)	8.47	5.76
Peak X Position (mm)	2.41	1.39
Peak X Velocity (mm/s)	0.0517	0.0299
Peak Yaw Body Rate (deg/s)	0.207	0.141

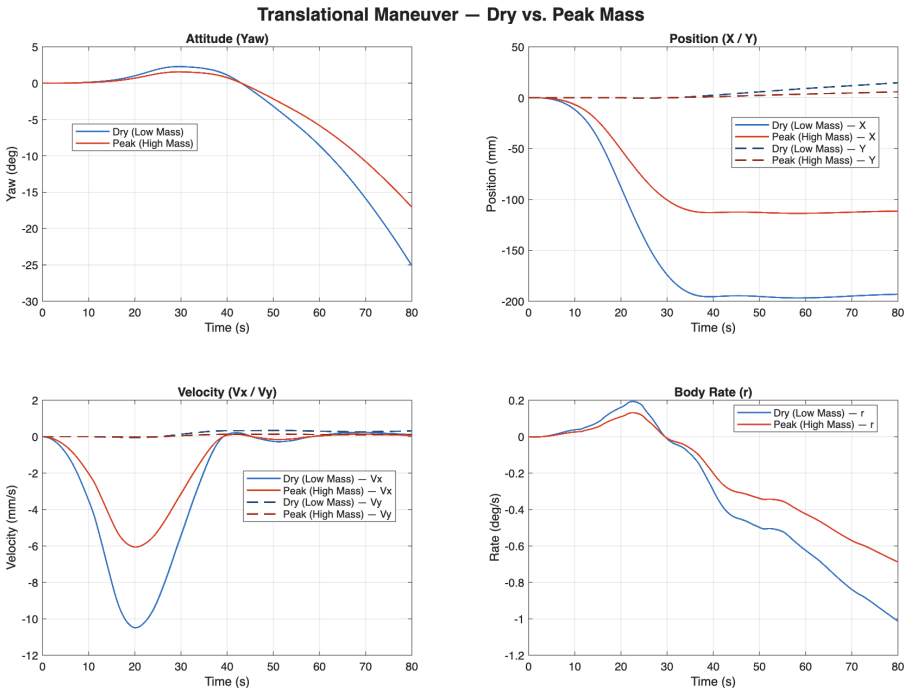

Figure 27: Translational Maneuver 6DOF response for Variable Satellite Mass

Table 4: Satellite attitude and positional response during the Translational Maneuver.

Metric	**Low Mass (118.5 kg)**	**High Mass (205 kg)**
Final Yaw (deg)	25.10	17.06
Peak X Position (mm)	196.7	113.6
Peak X Velocity (mm/s)	10.49	6.06
Peak Yaw Body Rate (deg/s)	1.01	0.69

The results indicate a significant correlation between system inertia and the magnitude of slosh-induced disturbances. For both the translational and reorientation maneuvers, the lower mass profile (118.5 kg) exhibited a 46% increase in both final yaw and peak body rate compared to the high-mass configuration (205 kg). Similarly, the reduction in system mass led to a 73% increase in peak X-position and peak X-velocity, which matches the ratio between the two mass profiles. These findings demonstrate that while the internal sloshing forces remain constant, the satellite's sensitivity to these perturbations is substantially heightened at lower mass profiles, providing a quantified result to the previously held assumption.

8.5 Comparative Analysis: Propellant Mass

In addition to the satellite's dry mass, the mass of the Xenon propellant is a critical variable. As propellant is gradually consumed throughout the mission, the changing fluid volume and distribution exert a significant influence on the overall sloshing dynamics. To quantify these effects, three discrete scenarios were analyzed based on the tank fill level:

- **High-Fill Scenario (70%):** Represents the early-mission stage with approximately 29 kg of liquid Xenon.
- **Baseline Scenario (50%):** Represents a mid-mission state with approximately 24 kg of liquid Xenon.
- **Low-Fill Scenario (30%):** Represents the late-mission stage with approximately 19 kg of liquid Xenon.

By evaluating these three cases, the sensitivity of the satellite's attitude control system can be characterized across the entire operational lifespan of the propellant supply.

Firstly, the CFD simulations yielded the slosh force, slosh moment, and the transient center of drift as follows:

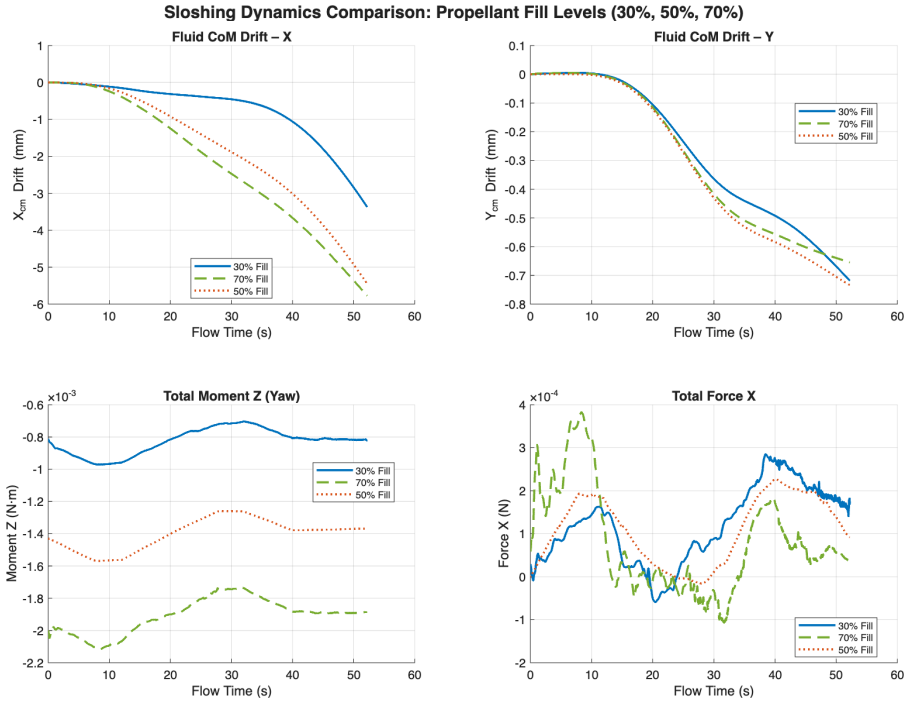

Figure 28: Fill Comparison CFD Outputs for Reorientation Maneuver

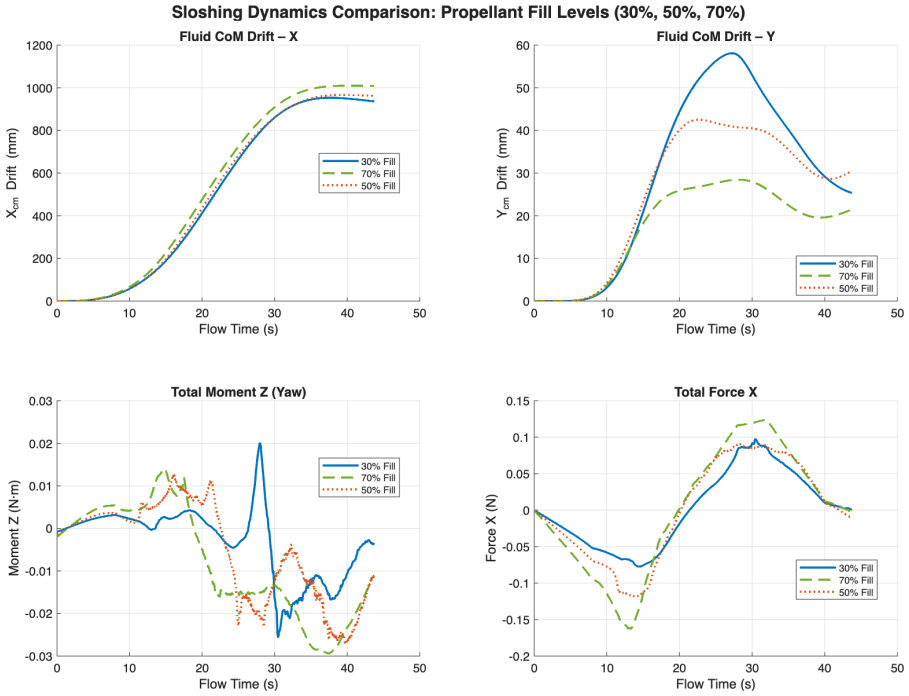

Figure 29: Fill Comparison CFD Outputs for Translational Maneuver

Utilizing the CFD results, the 6DOF analysis was repeated to determine the resulting attitude and torque responses. Due to the extensive simulation time required for each configuration, the comparison was conducted over a truncated simulation period. Nevertheless, the trends across the varying fill levels remain clearly visible and measurable.

Reorientation Maneuver:

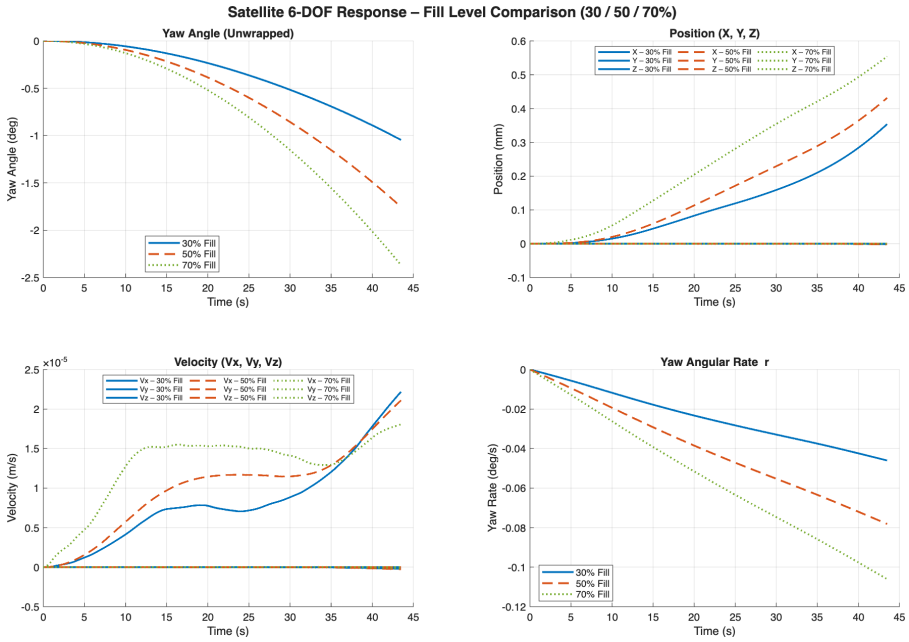

Figure 30: Fill Comparison 6DOF Analysis Outputs for Reorientation Maneuver

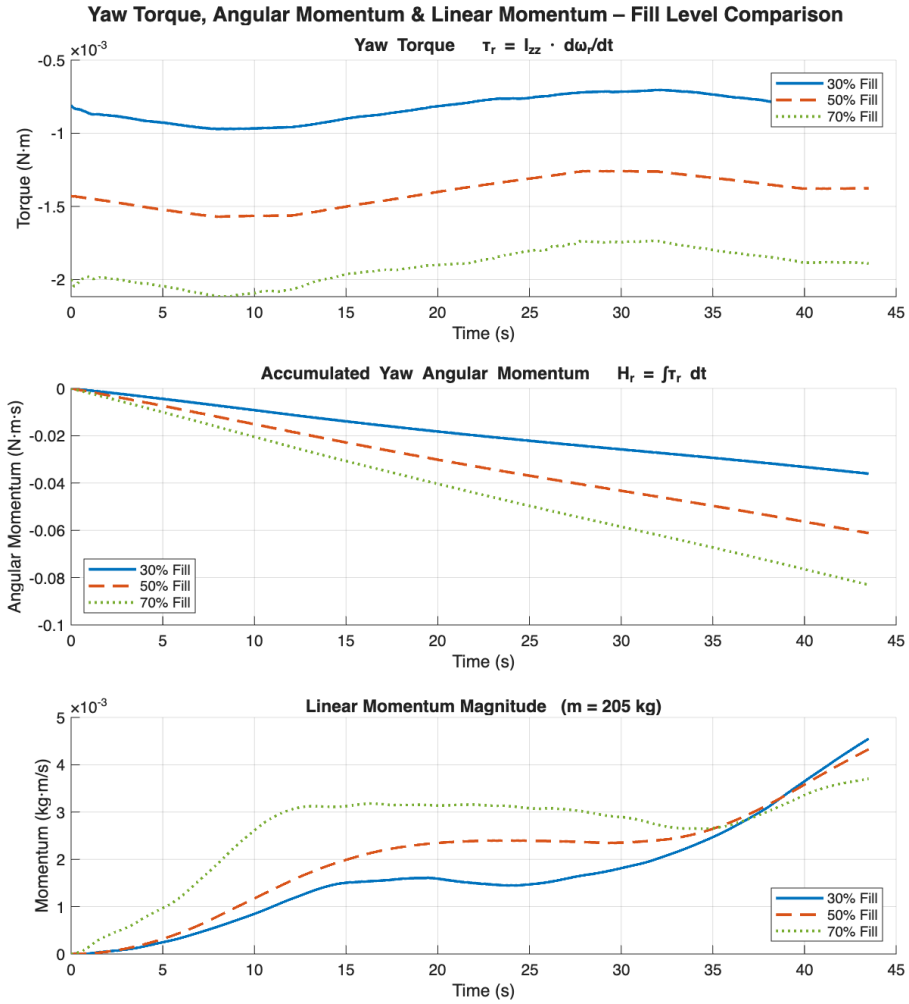

Figure 31: Fill Comparison Torque Outputs for Reorientation Maneuver

Translational Maneuver:

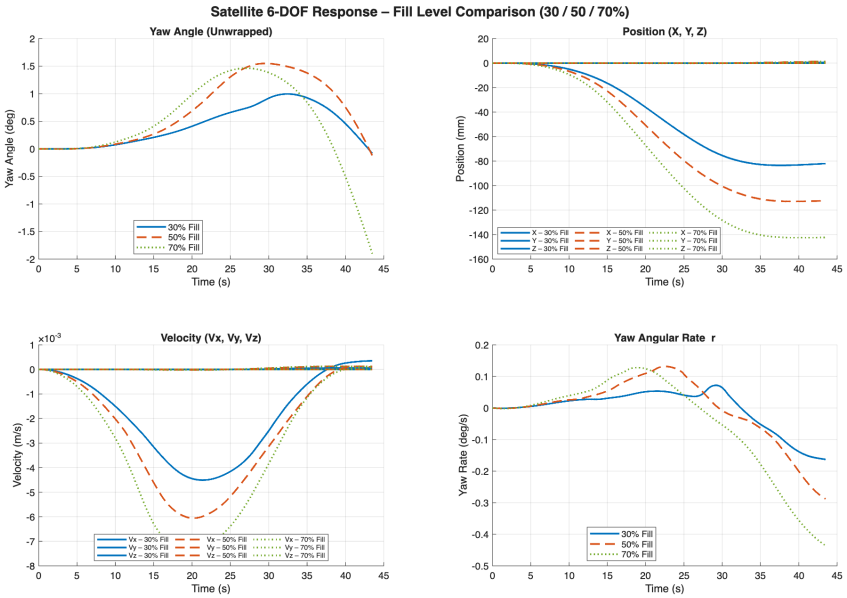

Figure 32: Fill Comparison 6DOF Analysis Outputs for Translational Maneuver

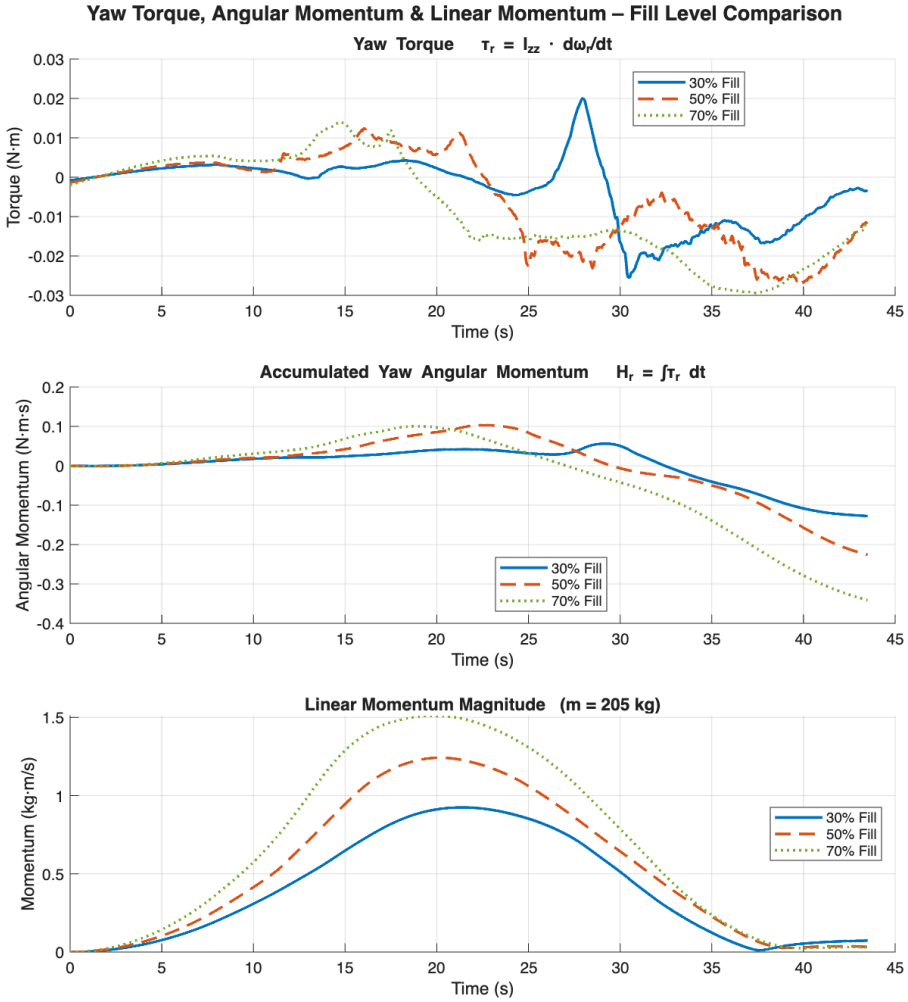

Figure 33: Fill Comparison Torque Outputs for Translational Maneuver

Figures 28 through 33 illustrate several critical trends. Primarily, higher fill ratios consistently yield greater slosh magnitudes and correspondingly higher attitude and torque responses. This correlation is fundamentally driven by the increased fluid mass, which generates greater forces and moments when subjected to the same acceleration profile.

A secondary trend is observed specifically within the translational maneuver. While positional drift follows the aforementioned mass-proportional trend, the attitude response exhibits a distinct temporal shift. Although the profiles for yaw angle, angular rate, and yaw torque maintain consistent geometries across all fill ratios, the onset of the response occurs earlier as the fill level increases. These trends are primarily driven by the higher natural frequency inherent to increased fill ratios, which results in a more rapid and "snappier" oscillatory response. Additionally, the reduced gas-regime volume in high-fill configurations ensures the fluid is in greater contact with the tank boundaries, allowing for an almost instantaneous and larger magnitude momentum transfer compared to the delayed wall impacts observed in lower-fill scenarios. While this phase shift has a negligible effect on the maximum instantaneous torque, it significantly influences the accumulated torque, resulting in higher total angular momentum for higher fill ratios.

8.5.1 Controllability

Despite these trends, the resulting sloshing effects remain within the controllable regime of the ARW-1A reaction wheel. To verify this, the peak and final state deviations for the 70% fill case representing the most demanding slosh scenario are compared against the reaction wheel's operational limits.

The maximum instantaneous torque for the 70% fill case is 0.0294 Nm. This represents an 8.9% increase over the baseline 50% fill value of 0.027 Nm, and remains well within the ARW-1A's maximum torque specification of 0.1 Nm.

The accumulated angular momentum requires a more nuanced comparison due to simulation constraints. While the baseline translational maneuver was analyzed over an 80-second duration, the comparative fill-level simulations were truncated at 43.5 seconds. At this 43.5-second mark, the 70% fill case yielded an accumulated angular momentum of 0.3412 Nms, an increase of $\Delta H = 0.1156$ Nms over the 50% fill case at the same timestamp. By applying this observed delta as a conservative offset to the original 80-second baseline value (0.5385 Nms), the projected total accumulated torque for a full 70% fill maneuver is approximately 0.6541 Nms. Even with this 21.5% increase, the requirement remains substantially below the reaction wheel's momentum storage capacity of 1.0 Nms.

Finally, the maximum linear momentum for the 70% case is 1.511 $\text{kg} \cdot \text{m/s}$, a 21.6% increase compared to the 50% fill baseline. Despite this rise in translational disturbance, the magnitude remains within the standard tolerance limits for a 200 kg-class satellite. Consequently, the proposed liquid-vapor storage regime is deemed mechanically controllable across all anticipated propellant fill levels.

9 Validation: design of an experiment

In this section, we present a preliminary experimental design aimed at validating the main CFD results. The objective is not to fully reproduce the space environment, but to recreate similar fluid dynamics in a controlled reduced-gravity setup and compare measurements with simulations.

9.1 Experimental objective and measurement principle

The first objective is to reproduce, as closely as possible, the geometry and volume used in the CFD study with a real tank filled with a representative liquid. This implies using a cylindrical tank of comparable dimensions and preserving the same configuration so that measured and simulated dynamics can be directly compared.

The tank is instrumented with flush-mounted pressure sensors distributed along the cylindrical wall. These sensors measure local wall pressure over time during fluid motion. A practical layout consists of several axial rings, each with uniformly spaced sensors. By combining and integrating these measurements over the wall, the resultant force and moment acting on the tank can be reconstructed. The experiment is therefore based on wall-pressure identification of sloshing loads.

9.2 Candidate reduced-gravity environments

Two main options were considered: parabolic flight and drop tower testing, each with different constraints.

9.2.1 Parabolic flight (Zero-G Flight)

Parabolic flight reproduces reduced gravity via a ballistic trajectory. Current Zero-G flights offer up to thirty parabolas of about 30 seconds each, totaling around fifteen minutes of reduced gravity. This enables repeated runs with reinitialization between parabolas, which is well suited for sloshing experiments.

The main drawback is cost. A typical research section costs around \$60k–\$70k, leading to an overall order of magnitude of \$70k–\$75k before hardware and travel.

9.2.2 Drop tower

Drop towers generate microgravity through free fall. NASA Glenn's facility offers 5.18 s of microgravity with residual acceleration below $10^{-5}g$. It supports payloads up to 455 kg and provides power, acquisition channels, and integration support.

The main advantage is the quality of microgravity and structured testing environment, with costs around \$5.8k per drop, significantly lower than parabolic flights for targeted tests.

The main limitation is duration. 5.18 s is much shorter than the CFD forcing window, making drop towers more suitable for early transient dynamics and first sloshing modes. The smaller

2.2 s tower further restricts payload size and duration but remains useful for early validation.

9.3 Preliminary payload architecture

The payload consists of five subsystems:

- a transparent cylindrical tank;
- a pressure sensor array;
- a linear excitation system;
- a structural interface;
- an outer enclosure.

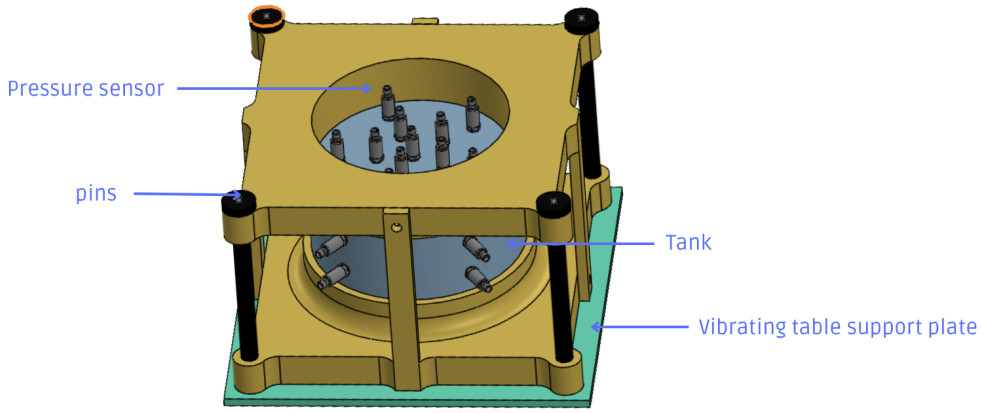

Figure 34: Detailed view of the tank module including sensors, pins, and vibrating support plate

The tank should remain transparent to allow visual observation. A clear polycarbonate cylinder is suitable due to its impact resistance and machinability. A representative geometry is 800 mm length, 200 mm diameter, and 10 mm thickness, giving about 20L volume.

A key design point is sensor integration. Threads in plastic are insufficient, so reinforced inserts or metallic interfaces are required for durability. Fabrication cost is driven by machining and integration, typically \$1,500–\$4,000.

The sensor array is central to the measurement strategy. Key requirements include compactness, wetted measurement, simple output, and robustness.

A low-cost PT506-type sensor enables early testing with large numbers at low cost. For a more robust setup, industrial sensors such as Dwyer 626/628 (\$149/unit) would increase total cost to about \$3,700, but improve reliability.

The tank is mounted on a linear shake table reproducing the CFD input. A rail-guided base driven by an actuator allows controlled motion along one axis and replay of deterministic profiles.

A custom rail-and-actuator system is preferred over expensive commercial stages. A typical budget is around $2,000.

A rigid interface connects the tank to the moving plate, ensuring proper transmission of acceleration without parasitic motion. Simple clamping saddles or brackets can be used. This subsystem is low-cost and can be 3D printed.

The payload is enclosed in a rigid box to ensure protection, containment, and structural support. An aluminum frame with transparent panels is suitable. Cost remains in the low hundreds of dollars.

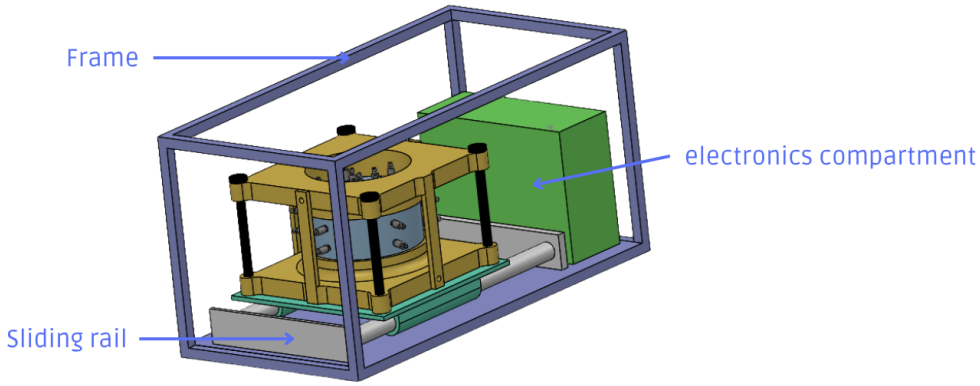

Figure 35: Complete assembly of the test bench with frame, linear guide, and embedded electronics

9.4 Embedded electronics and data acquisition

The system must allow real-time monitoring of pressure channels and motion input. The architecture includes:

- a 24 VDC supply;
- current-to-voltage conversion;
- a multichannel DAQ;
- a motion controller;
- an embedded controller if needed.

A practical approach uses shunt resistors for 4–20 mA sensors with standard USB DAQ devices. MCC hardware and NI FlexLogger enable fast deployment without custom software.

A staged approach is recommended: first use vendor tools, then develop custom software only if needed. Cost is minimized by keeping the DAQ architecture simple.

9.5 Impact of the test platform on payload constraints

9.5.1 Case 1: parabolic flight

The payload must operate safely in a crewed aircraft with repeated gravity transitions. This requires strong containment, restrained components, moderate mass, and easy reset between runs.

The advantage is the ability to perform multiple tests, making it suitable for full time-history comparison with CFD.

9.5.2 Case 2: drop tower

The payload must be autonomous and structurally robust to survive high deceleration (up to $65g$). It must include onboard power, data logging, and comply with vacuum constraints when required.

This leads to compact, highly constrained designs focused on short-duration measurements. Drop towers are ideal for early validation and transient analysis, but not for full maneuver reproduction.

9.6 Development logic

A progressive approach is recommended. First, build a laboratory demonstrator with a simplified tank, limited sensors, and basic excitation and DAQ. This validates the measurement concept at moderate cost.

Then, depending on objectives, either proceed to parabolic flight for long-duration validation or to drop-tower testing for short-time reduced-gravity response and payload robustness.

10 Economic Impact and Trade-Off Analysis

This section evaluates the economic implications of storing Xenon propellant in liquid–vapor equilibrium as an alternative to traditional supercritical storage. To determine the practical viability of allowing a sub-cooled system, the analysis focuses on the trade-off between continuous thermal energy savings and the transient mechanical power penalties associated with propellant sloshing. The objective is to quantify the net impact of these competing factors over an orbital cycle of the satellite.

The study is structured around two distinct operational cases:

Case 1: Traditional Supercritical Storage (Industry Standard) The Xenon is maintained at a constant temperature above its critical point ($T_{sc} = 21°\text{C}$). This baseline approach requires a continuous power draw for thermal regulation but ensures the propellant remains a single-phase fluid. Consequently, no sloshing occurs, and the ARW-1A reaction wheels operate at a steady-state power level without requiring additional energy for attitude stabilization.

Case 2: Liquid–Vapor Equilibrium Storage The propellant is permitted to enter a liquid–vapor regime at a lower equilibrium temperature ($T_{l/v} = -3°C$). While this significantly reduces the heating budget due to the lower thermal gradient, the presence of a two-phase fluid introduces sloshing disturbances during maneuvers. As a result, the reaction wheels must expend additional energy to maintain satellite orientation, representing a transient power penalty.

By establishing these parameters, a thermal analysis can be performed to identify the point at which the thermal energy saved in Case 2 justifies the mechanical energy costs. This comparison provides the technical basis for potential optimizations in power subsystem sizing and overall mission return on investment.

10.1 Heating energy consumption over mission life and pressure vessel constraints

During a typical low Earth orbit cycle, satellite surface temperature varies significantly due to radiation intensity and orientation. As a result, internal components must tolerate a wide temperature range to remain functional. Although the surface ranges from -170°C to +120°C per orbit [15], internal electronics typically operate between -20°C and +50°C [16]. Therefore, for the purpose of the study, heat transfer will be monitored between the propellant tank, which is assumed to have its own heat controller, and the internal equipment of the satellite. A simp

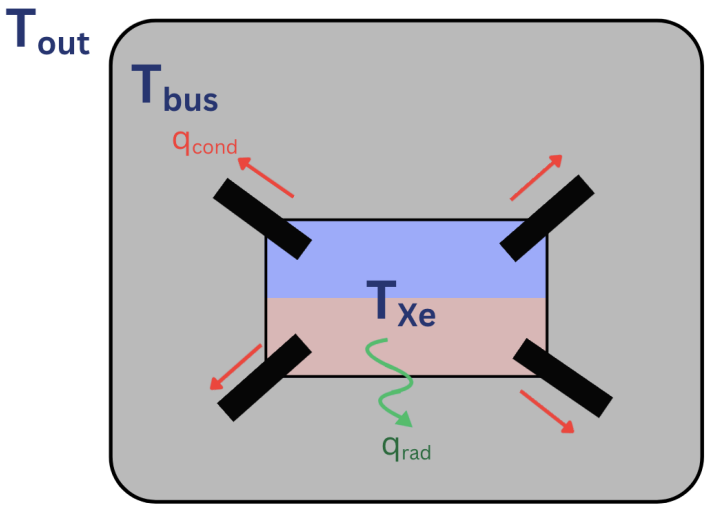

Figure 36: Heat Transfer Model

Using the heat model shown,

$$m_{\text{prop}} c_p \frac{dT}{dt} = q_{\text{in}} - q_{\text{loss}}$$

Due to the propellant tank being inside the body of the satellite, there are two primary ways heat is being transferred out. The first is radiation loss, while the second is conduction. For the radiation, the propellant tank is likely coated with a Multi-Layer Insulation. Therefore,

the emissivity value can be approximated to $\epsilon = 0.018$. For the conduction, we assume that the propellant tank is connected to the rest of the satellite using four Titanium Struts. These struts would each have a cross-sectional area of $1cm^2$ and a clearance length of 3 cm. The thermal conductivity of Ti-6Al-4V Titanium is 6.7 W/M-K.

$$q_{\text{rad}} = \epsilon\sigma A_{\text{sat}} \left(T^4 - T_{\text{bus}}^4\right) \qquad q_{\text{cond}} = \frac{kA_{struts}}{L} \left(T - T_{\text{bus}}\right)$$

At steady state ($dT/dt \approx 0$):

$$P_{\text{heating}} = q_{\text{loss}} = q_{\text{rad}} + q_{\text{cond}}$$

These equations were evaluated in several conditions. Three bus temperatures were used. These account for the high end, low end, and average internal temperature. For each bus temperature, the heating power was found for both the supercritical case and the liquid/vapor case:

Table 5: Steady-State Heating Power Requirements for Xenon Propellant Tank

Internal Bus Temperature	**Supercritical (T_{sc}) Heating Power [W]**	**Liquid/Vapor ($T_{l/v}$) Heating Power [W]**
High End (50°C)	0.0000	0.0000
Average (15°C)	0.7832	0.0000
Low End (-20°C)	5.0730	2.0092

While initial estimates placed the heating power for the industrial case at approximately 5 Watts, real-world data provided by Airbus US suggest that this figure is conservative. Under peak summer conditions, power consumption can reach between 8 to 10 Watts, totaling up to 50 kJ of energy per 90-minute orbital cycle.

However, for the purpose of this study and to establish a consistent baseline for energy efficiency, the model is used and assumes that the satellite maintains a steady average internal bus temperature of 15°C throughout the cycle. Under these standardized conditions, the total energy saved per orbital period was calculated as $\Delta E = 4229.34$ J using the equation below.

$$\Delta E = \int \left(P_{heating}(T_{sc}) - P_{heating}(T_{lv})\right) dt$$

10.2 Control system energy consumption over mission life

It is also necessary to determine the extra power used by the ARW-1A reaction wheel to account for propellant sloshing when the Xenon is in a liquid state. The reaction wheel utilizes 10 W of steady-state power and reaches up to 100 W at maximum torque (0.1 N·m).

To estimate power consumption across varying loads, a simple linear model was employed. This model was deliberately selected to provide a conservative upper-bound approximation. While

real-world power draw typically exhibits a more exponential relationship at higher torque levels, the linear approach ensures a larger safety margin, preventing an underestimation of energy requirements during peak maneuvers. Detailed power usage estimates for both maneuvers are illustrated in Figures 30 and 31.

$$P_{slosh-induced} = \frac{P_{max} - P_{steady}}{\tau_{max}} * \tau_{slosh}$$

$$P_{total} = P_{steady} + P_{slosh-induced}$$

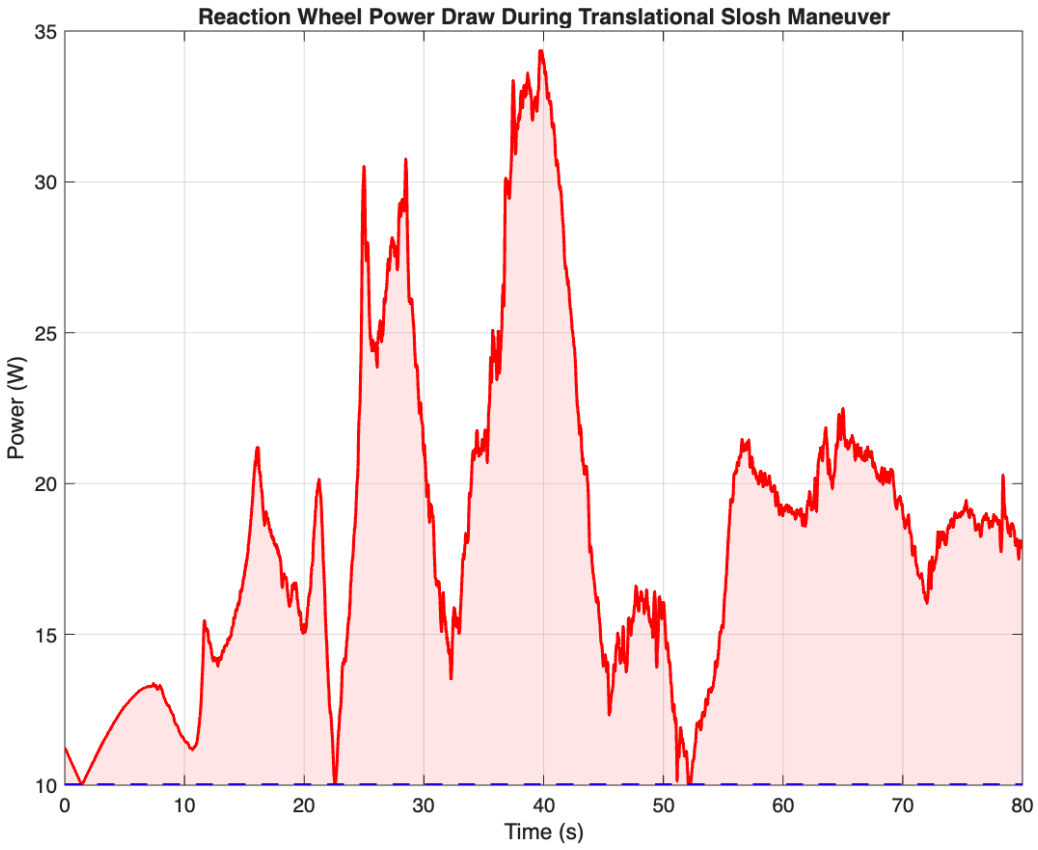

Figure 37: Power Usage during Translational Maneuver

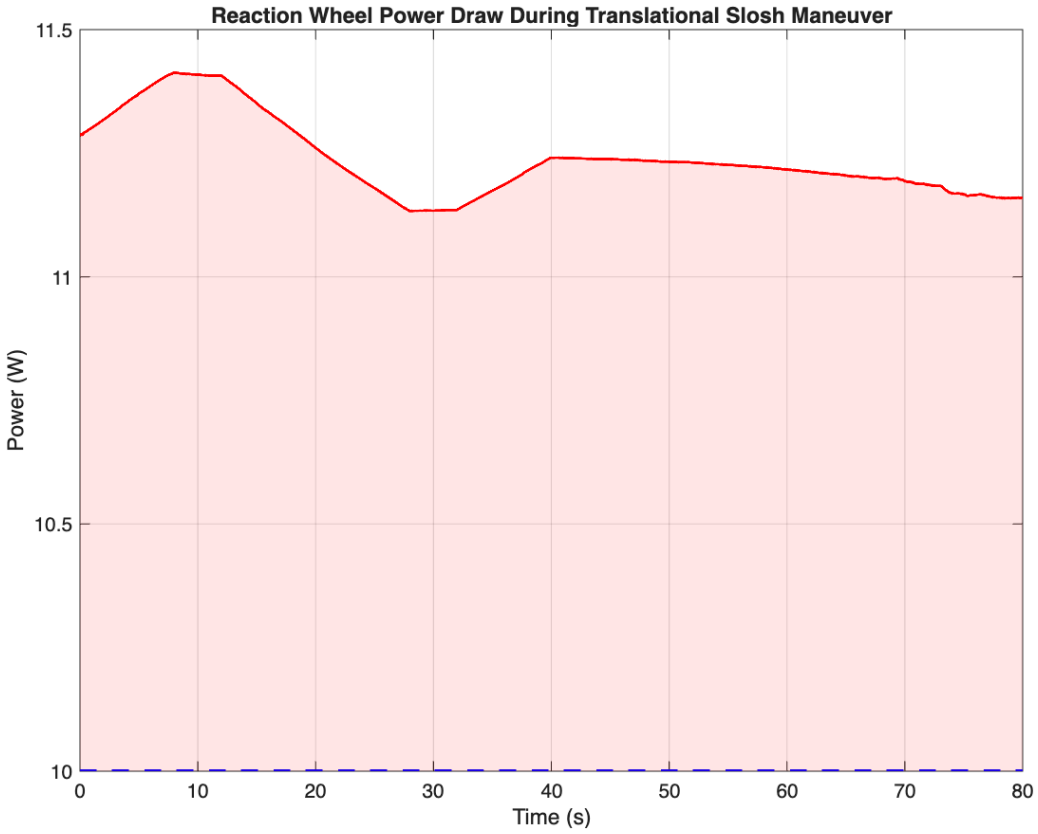

Figure 38: Power Usage during Rotational Maneuver

From the figures shown above, the average watt consumption and total energy cost for the maneuvers was determined and shown in Table 4 below.

Table 6: Summary of Additional Power and Energy Requirements for Slosh Maneuvers

	Translational Maneuver	**Rotational Maneuver**
Average Power Consumption [W]	8.43	1.24
Energy Cost for Maneuver [J]	674.09	99.13

Based on the Energy Cost per Maneuver, the Translational Maneuver can occur 6.27 times before breaking even with the energy saved through heat transfer over a single 90-minute orbital cycle. The Rotational Maneuver, on the other hand, can occur over 42 times before breaking even. These values show that operating the reaction wheel requires more instantaneous energy than heating the Xenon to a supercritical states. However, in a typical satellite operation, these maneuvers tend to occur infrequently. Translational Maneuvers tend to occur only a few times a month, as satellites tend to wait for the orbit to decay for a few kilometers before activating the maneuver. On the other hand, rotational maneuvers occur a few times per orbit, but require significantly less energy to operate.

10.3 Economic Profit

By allowing the Xenon propellant to enter the liquid regime, a satellite avoids the continuous power drain required to regulate the propellant's temperature at a supercritical state. This is

especially significant considering the severe constraints and high cost of energy generation in space. In satellite systems engineering, power is directly tied to mass and revenue. Because the transient power penalty of the reaction wheels is vastly outweighed by the continuous thermal savings, the satellite's overall power budget operates at a net surplus.

This surplus translates directly into economic profit. During the design phase, engineers can downsize the solar arrays and batteries to save significant mass and launch costs. Alternatively, if the power system size is maintained, the saved energy can be redirected to the primary payload, directly increasing data throughput and revenue generation over the mission's lifetime.

Furthermore, sub-cooled liquid Xenon is significantly denser than supercritical Xenon. This phase change allows a higher mass of propellant to be stored within the same tank volume at a lower operating pressure. This increased capacity extends the satellite's operational lifespan, splitting initial manufacturing and launch costs over a longer period and drastically improving the mission's return on investment.

11 Conclusion

This study set out to evaluate the feasibility and implications of storing xenon in liquid form for electric-propulsion satellites operating in microgravity. Through a combination of analytical modeling, numerical simulations, and experimental design considerations, the project provides a comprehensive framework for understanding this complex problem.

The results demonstrate that sloshing behavior is highly dependent on the type of maneuver and corresponding force regime. Simplified analytical models, particularly the equivalent mechanical approach, proved effective in capturing the dominant dynamics, for linear responses and were validated through a numerical simulation campaign. A nonlinear limit was also established semi-empirically and proved reliable on multiple simulations.

The attitude analysis definitively established that slosh-induced disturbances remain well within the controllable limits of the ARW-1A reaction wheel. To substantiate this finding, two comparative sensitivity analyses were performed: the first examined the impact of satellite mass and inertia, while the second evaluated the effects of propellant fill levels at 30%, 50%, and 70%. Lower-mass states and higher fill ratios were found to increase the satellite's sensitivity to perturbations, resulting in higher magnitudes of positional and attitude drift. However, all critical metrics, including instantaneous torque and accumulated angular momentum, consistently remained below established engineering thresholds.

For the economic analysis, the comparison between liquid and supercritical xenon storage reveals a fundamental trade-off: liquid storage introduces dynamic slosh uncertainties, whereas supercritical storage simplifies fluid behavior at the cost of continuous, expensive thermal regulation. However, because thermal energy savings drastically outweigh transient attitude control penalties, liquid storage ultimately yields a net power surplus thus increasing volumetric efficiency, extending mission lifespan, and maximizing the overall economic return on investment.

Finally, the proposed experimental setup provides a realistic pathway for validating the models under reduced-gravity conditions, which is essential for bridging the gap between theory and real-world application.

Future work would mainly focus on the experiment, finishing its design and manufacturing parts. Some additional work is also needed for the numerical simulations, the 3D cases need to be fully simulated and understood in order to get more reliable results.

12 Bibliography

[1] "Electric Propulsion: The Engine Driving the Next Era of Spacecraft Growth," Space Insider, Nov. 29, 2025.

[2] H. N. Abramson, Ed., The Dynamic Behavior of Liquids in Moving Containers, with Applications to Space Vehicle Technology. Washington, DC, USA: NASA, 1966.

[3] F. T. Dodge, The New "Dynamic Behavior of Liquids in Moving Containers". San Antonio, TX, USA: Southwest Research Institute, 2000.

[4] NASA, Space Vehicle Design Criteria (Structures): Propellant Slosh Loads. Washington, DC, USA: NASA, Aug. 1968.

[5] R. J. Hung and H. L. Pan, "Mathematical model of bubble sloshing dynamics for cryogenic liquid helium in orbital spacecraft dewar container," Advances in Space Research, vol. 31, no. 8, pp. 1983–1993, Apr. 2003, doi: 10.1016/S0273-1177(03)00170-6.

[6] R. J. Hung, H. L. Pan, and Y. T. Long, "Sloshing dynamics modulated cryogenic helium fluids driven by gravity gradient or jitter accelerations associated with slew motion in microgravity," Acta Mechanica Sinica, vol. 10, no. 4, pp. 315–328, Nov. 1994.

[7] A. Rafiee, F. Pistani, and K. Thiagarajan, "Study of liquid sloshing: Numerical and experimental approach," Computational Mechanics, vol. 47, no. 1, pp. 65–75, Jan. 2011, doi: 10.1007/s00466-010-0529-6.

[8] H. Q. Yang and J. Peugeot, "Propellant sloshing parameter extraction from CFD analysis [Extended Abstract]," presented at the AIAA Joint Propulsion Conference, Nashville, TN, USA, Jul. 25–28, 2010.

[9] G. Schmidt, "Electric propulsion research and development," NASA NTRS, 2018.

[10] Y. Zhao, L. Sun, X. Yu, et al., "Supercritical Xe as Propellant in Satellite Electric Propulsion System: Experimental Study on Thermal Physical Properties," IOP Conf. Ser.: Mater. Sci. Eng., 2019.

[11] R. W. Warner and J. T. Caldwell, Experimental Evaluation of Analytical Models for the Inertias and Natural Frequencies of Fuel Sloshing in Circular Cylindrical Tanks. Washington, DC, USA: NASA, May 1961.

[12] R. A. Ibrahim, *Liquid Sloshing Dynamics: Theory and Applications*. Cambridge, U.K.: Cambridge University Press, 2005.

[13] Airbus U.S. Space Defense, *ARROW Brochure*. Airbus U.S. Space Defense, 2021.

[14] V. K. Rawlin, M. J. Patterson, and R. P. Gruber, *Xenon Ion Propulsion for Orbit Transfer*. Cleveland, OH: NASA Lewis Research Center, 1990.

[15] Blueshift Materials, *Staying Cool: How Satellites Survive the Temperature Extremes of Space*. Blueshift Materials

[16] H. Sundu and N. Döner, *Detailed Thermal Design and Control of an Observation Satellite in Low Earth Orbit*. European Mechanical Science, 2020.